RSC Advances

PAPER

View Article Online
View Journal | View Issue

Cite this: *RSC Adv.*, 2025, **15**, 27369

Alkyl pyridine ionic liquid as a green corrosion inhibitor for mild steel in acidic medium

Fang Luo,[a] Pei Yao,[b] Jiale Zhang[a] and Entian Li *[a]

Received 11th June 2025
Accepted 22nd July 2025

DOI: 10.1039/d5ra04148a

rsc.li/rsc-advances

Using electrochemical measurements, the corrosion inhibition performance of pyridine bromide ionic liquid corrosion inhibitors on low carbon steel was evaluated under different concentrations and alkyl chain lengths of anions. The optimal process conditions were obtained: at 25 °C, in a 1 M HCl corrosion medium, the 1-dodecyl-3-methylpyridine bromide ionic liquid ($[C_{12}Py]Br$) exhibited the best corrosion inhibition effect, with maximum inhibition rates of 94.1%. The study mechanism showed that the adsorption process was a mixed adsorption dominated by chemical adsorption. Surface analysis (SEM/EDS, XPS) and quantum chemistry results verified that $[C_nPy]Br$ could form a protective film on the surface of low carbon steel and inhibit its corrosion. In addition, molecular dynamics simulations were used to analyze the adsorption behavior of corrosion inhibitor molecules on the Fe(110) surface, and the formation sequence of bond and non-bond interactions in the Fe corrosion inhibitor molecular system on the Fe(110) surface was obtained, which was consistent with the experimentally determined corrosion inhibition efficiency. The radial distribution function (RDF) showed that the adsorption mode of the corrosion inhibitor on the metal surface was a mixed adsorption dominated by chemical adsorption and supplemented by physical adsorption.

1 Introduction

Mild steel is widely employed in various industrial applications, including pipeline construction for oil and gas transportation, acid descaling, and acid pickling. This preference is due to its abundant availability, favorable physicochemical properties, and cost-effectiveness. On the other hand, when subjected to aggressive acidic environments, particularly hydrochloric acid used in cleaning and descaling processes, this material is highly susceptible to corrosion, potentially resulting in significant economic losses and safety hazards. As a result, this problem has attracted considerable attention from many researchers because of its seriousness and consequences.[1,2] The industrial sector has adopted a variety of metal corrosion prevention techniques to mitigate the adverse effects of metal corrosion. Among these methods, the use of corrosion inhibitors stands out as an exceptionally effective means of safeguarding metals against corrosion in a diverse array of complex environmental conditions. This approach is highly valued for its numerous advantages, such as its cost-effectiveness, broad adaptability, and ease of implementation.[3]

The use of corrosion inhibitors in a corrosive environment effectively prevents severe damage caused by corrosion on metal surfaces. Corrosion inhibitors exhibit water solubility and maintain thermal stability even in highly aggressive acidic environments. These compounds can interact with metallic ions to create a metal-inhibitor complex that remains chemically, thermally, and thermodynamically stable, particularly in acidic environments.[4] Next, the resulting complex is efficiently adsorbed onto the metal surface, creating a stable thin film that serves as a protective barrier, effectively isolating the metal from the corrosive environment. As a result, the protective film provides significant defense for the metallic surface, shielding it from corrosion processes effectively. The performance of corrosion inhibitors is attributed to their heteroatoms, such as nitrogen, oxygen, phosphorus, and sulfur, as well as their polar functional groups ($-C{=}N-$, $-NH_2$, $-OH$, $-OCH_3$, $-SH$).

In the processes of adsorption and inhibition, the π-electrons of aromatic rings and lone p-electrons from heteroatoms are transferred into the empty d-orbitals of iron, forming strong covalent bonds.[5] However, numerous organic compounds containing heteroatoms like phosphorus, oxygen, nitrogen, and sulfur have been identified as potential alternatives to toxic corrosion inhibitors. Consequently, a key area in contemporary corrosion inhibitor research is the development of innovative and eco-friendly solutions.[6,7]

A considerable number of researchers focus on utilizing environmentally friendly corrosion inhibitors, including natural extracts, pharmaceutical compounds, ionic liquids (ILs), and similar substances. In recent years, ionic liquids (ILs) have garnered significant interest owing to their distinctive

---

[a] School of Petroleum Engineering, Changzhou University, Wujin District, Changzhou 213164, Jiangsu, PR China. E-mail: let@cczu.edu.cn

[b] Department of Chemistry and Materials Engineering, Changzhou Vocational Institute of Engineering, Changzhou 213164, Jiangsu, PR China

characteristics, including minimal toxicity, high polarity, non-flammability, low vapor pressure, remarkable solubility, and exceptional thermal stability.[1] In addition, their adjustable properties enable the creation of various "custom-designed" functional ionic liquids (ILs) tailored for specific applications and materials. For instance, the anti-corrosion properties of ionic liquids (ILs) can be tailored at the molecular level to safeguard materials with specific compositions, thereby enhancing the efficiency of inhibition.[8] Among these compounds, imidazolium-based ionic liquids (ILs) with carbon chains of varying lengths have been suggested as effective candidates for corrosion inhibition. This is attributed to the aromatic ring, which serves as the bonding site between the metallic surface and the ILs.[9,10] Conversely, the carbon chain tail contributes to the formation of a hydrophobic layer, which aids in protecting metallic surfaces by providing adequate coverage. For example, S. Shuncun *et al.*[11] investigated how the length of the alkyl chain attached to the imidazolium ring in novel ionic liquids (ILs) influenced their corrosion inhibition performance in acidic solutions. They found that the inhibition efficiency improved as the carbon chain length of the alkyl group increased. They concluded that as the carbon chain length of the alkyl group increased, the inhibition efficiency also improved. In the study by Azeez *et al.*,[12] three environmentally friendly ionic liquids (ILs)—1-methyl-3-propylimidazolium iodide (MPIMI), 1-butyl-3-methylimidazolium iodide (BMIMI), and 1-hexyl-3-methylimidazolium iodide (HMIMI)—were evaluated as inhibitors to reduce mild steel corrosion in a 1 M HCl solution.

Moreover, since pyridine-based ILs also have an aromatic ring, the corrosion inhibition effect of pyridine-based ILs corrosion inhibitors mild steel has been increasingly reported. In the study by Bousskri *et al.*,[13] the protection of mild steel against corrosion in 1 M HCl was examined in the presence and absence of different concentrations of 1-(2-(4-chlorophenyl)-2-oxoethyl) pyridazinium bromide (CPEPB). The findings indicate that CPEPB is an effective inhibitor, with the inhibition efficiency reaching 91% at a concentration of 10^{-3} M. Despite the fact that existing studies have revealed the possible mechanisms of corrosion inhibition through various technical means, there is still a lack of in-depth analysis of the interaction between pyridine-based ILs corrosion inhibitors and metal surfaces, especially the impact of the molecular structure of the corrosion inhibitor on its performance.[14,15]

Due to the structural tunability and validated physicochemical stability of [C_nPy] Br ionic liquids, we chose them. Pyridine based ionic liquids, such as [C_nPy] Br, have excellent corrosion inhibition potential due to the strong adsorption promoted by π electrons through aromatic pyridine rings, and the hydrophobicity and surface coverage regulated by alkyl chains. Systematically changing the alkyl chain length ($n = 4, 8, 12$) can clearly understand the relationship between molecular structure and inhibitory performance. This design draws on the best case of pyridine based ionic liquids in the field of corrosion, such as Alrefaee *et al.*'s[16] report that 1-dodecylpyridin-1-ium bromide (Pyr-C_{12}-Br) has a corrosion inhibition rate of over 91% on low carbon steel in 1 M HCl. Prior studies confirm pyridinium ILs achieve >90% inhibition in acidic media (*e.g.*, Bousskri *et al.* reported 91% for CPEPB in 1 M HCl[17]), yet none systematically investigated alkyl chain length effects on mild steel.

The synthesis of [C_nPy] Br adopts a single step quaternization reaction (3-methylpyridine + bromoalkane) with a yield of >90%. This route conforms to the principles of green chemistry and avoids complex purification steps. Given its high efficiency, tunable structure, and low toxicity, [C_nPy]Br holds promise for applications in industrial cooling water systems, oilfield acidizing processes, and metal processing, addressing the urgent need for sustainable corrosion inhibitors. Internationally, pyridinium ILs show promise in: oil/gas pipelines: Saudi Aramco field tests reduced corrosion rates by 94% in acidizing fluids;[18] metal processing: Chinese steel mills adopted similar ILs for pickling baths, cutting waste treatment costs by 40%.[19]

In this study, mass loss tests and surface analysis techniques (scanning electron microscopy (SEM) and X-ray photoelectron spectroscopy (XPS)) were employed to assess the corrosion inhibition performance of [C_nPy]Br ionic liquids on mild steel in 1 M HCl. The corrosion resistance properties and mechanisms of [C_nPy]Br ionic liquids were further investigated using potentiodynamic polarization measurements (PDP) and electrochemical impedance spectroscopy (EIS). Lastly, the proposed corrosion inhibition mechanism was confirmed by adsorption analysis (adsorption isotherm model and quantum chemical calculations) and molecular dynamics simulations.

2 Experimental

2.1 Reagents

Mackin provided 3-methylpyridine, 1-bromobutane, 1-bromooctane, and 1-bromododecane, while Sinopharm Chemical Reagents Co., Ltd provided ethyl acetate, potassium bromide, and acetone. Hydrochloric acid and anhydrous ethanol were purchased from Jiangsu Yongfeng Chemical Reagent Co., Ltd. The details regarding the specifications and origins of the main reagents employed in this experiment are outlined in Table 1.

2.2 Synthesis and characterization of [C_nPy]Br

Following the procedure reported in ref. 20 and 21, three [C_nPy] Br compounds were synthesized. Firstly, accurately weighed 9.91 g 3-methylpyridine and 15.07 g 1-bromobutane (or 21.24 g 1-bromooctane, 27.41 g 1-bromododecane) in a molar ratio of 1 : 1.1. Subsequently, 3-methylpyridine was introduced into a three -necked flask, and the precisely weighed 1-bromobutane (or 1-bromooctane, 1-bromododecane) was slowly added to it. Utilizing a condensation reflux to prevent the wastage of reactants and to ensure an air-free environment during the reaction, the reaction was stirred at 70 °C for a duration of 4 h. The resulting liquid was washed several times with anhydrous ethanol (50 ml) to remove unreacted starting material, followed by rotary evaporation at 60 °C to remove residual ethanol and subsequent drying in a vacuum oven at 60 °C for more than 12 h to obtain the pure [C_nPy]Br product (Fig. 1).

The characterization of the synthesized products was conducted with a Thermo Scientific Nicolet iS50 FT-IR, as

Table 1 Table of reagent and drug details

Chemical reagents	Providers	Purity
3-Methylpyridine	Macklin	≥99%
1-Bromobutane	Macklin	≥99%
1-Bromooctane	Macklin	≥98%
1-Bromododecane	Macklin	≥98%
Ethyl acetate	Sinopharm Chemical Reagents Co., Ltd	≥99.5%
Potassium bromide	Sinopharm Chemical Reagents Co., Ltd	≥99%
Acetone	Sinopharm Chemical Reagents Co., Ltd	≥99.5%
Hydrochloric acid	Jiangsu Yongfeng Chemical Reagent Co., Ltd	37%
Anhydrous ethanol	Jiangsu Yongfeng Chemical Reagent Co., Ltd	≥99.5%

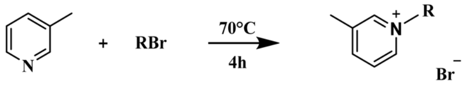

Fig. 1 Synthesis path of [C$_n$Py]Br ILs.

illustrated in Fig. 2. The peak observed at 3419 cm^{-1} is a water peak caused by moisture absorption. The peak at 3032 cm^{-1} is the result of the C–H stretching vibration of the pyridine aromatic ring. The peak at 2928 cm^{-1} is caused by C–H stretching vibrations of methyl groups.[22,23] The peaks at 1633 cm^{-1} and 1492 cm^{-1} can be attributed to the stretching vibrations of C═N and C═C in the pyridine aromatic ring, respectively. Asymmetric stretching vibration of methyl and methylene groups leads to the appearance of peak 1492 cm^{-1} (ref. 24). A peak observed at 1143 cm^{-1} indicates the in-plane deformation vibration of the C–H bond on the pyridine ring; an absorption peak around 1358 cm^{-1} confirms the presence of carbon–nitrogen single bonds. The increasing intensity of the hydroxyl peak at 3419 cm^{-1} with longer carbon chains is primarily attributed to the enhanced intermolecular hydrogen bonding. As the alkyl chain length increases, the hydrophobic effect promotes the aggregation of pyridinium cations, leading to a higher local concentration of hydroxyl groups from absorbed water molecules. This aggregation facilitates stronger hydrogen bonding networks, resulting in a more pronounced hydroxyl stretching vibration peak. Additionally, the increased molecular weight and surface area of longer-chain compounds may enhance water adsorption capacity, further contributing to the observed peak intensity increase. The presence of these spectral bands offer initial confirmation that the synthesis of compound [C$_n$Py]Br has been successfully achieved.

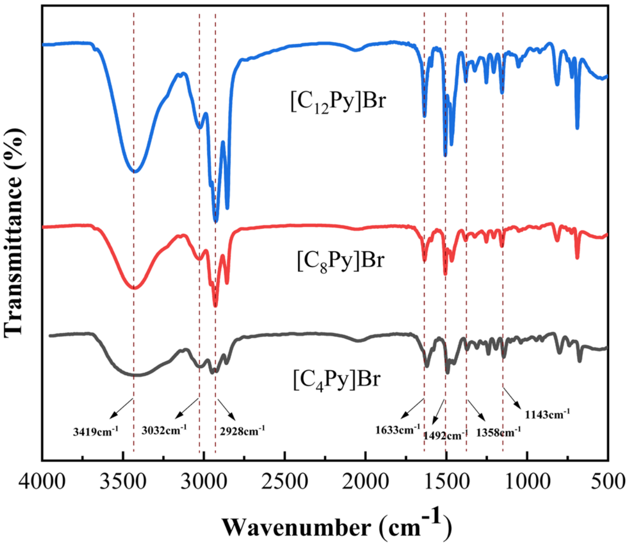

Fig. 2 FT-IR spectrum of [C$_n$Py]Br.

2.3 Materials preparation

The experimental specimens were Q235 carbon steel samples, characterized by dimensions of 25 mm × 15 mm × 2 mm. A comprehensive summary of the elemental composition and their respective percentages in the mild steel is presented in Table 2. Prior to experimentation, the samples underwent a meticulous surface preparation process. They were initially abraded with emery paper grades ranging from 400 to 1200, ensuring a smooth and mirror-like finish. Subsequently, the samples were degreased using ethanol, followed by thorough rinsing with distilled water. The samples were dried using a warm air stream and then placed in a desiccator for storage until needed.[25] For the electrochemical testing, the samples were precisely cut into smaller pieces measuring 10 mm × 10 mm × 2 mm. Copper wires were firmly attached to the inactive surface of the test specimen through welding to prepare the working electrode. The assembly was then carefully embedded in epoxy resin, ensuring an exposed geometric area of 1 cm^2 for the electrode. This meticulous preparation was crucial for the accurate and reliable conduct of the electrochemical tests.[3]

A 1 M HCl solution was made by mixing concentrated hydrochloric acid (37%) with purified water. Corrosion inhibitors were introduced into the 1 M HCl solution to create test solutions with inhibitor concentrations ranging from 0.25 mmol L^{-1} to 8 mmol L^{-1}.

Table 2 The composition and weight percentages of the elements in the mild steel (wt%)

C	Si	Mn	P	S	Fe
0.18	0.30	0.32	0.04	0.03	Balance

2.4 Weight-loss method

The corrosion resistance characteristics of the synthesized [C$_n$Py]Br were assessed using a mass loss experiment. The newly prepared mild steel samples were measured and immersed in the solution for approximately 8 h, both with and without different concentrations of [C$_n$Py]Br. After the immersion process, the mild steel samples were taken out of the test solutions, washed thoroughly with deionized water, dried with warm air, and carefully weighed. To calculate the mean weight loss, each test was conducted in triplicate.[26] The samples' weight loss was measured at temperatures of 298 K, 308 K, 318 K, and 328 K, respectively. The following equations can be used to determine the corrosion rate and the efficiency of corrosion inhibition:

$$C_\mathrm{R} = \frac{m_1 - m_2}{s \times t} \tag{1}$$

$$\theta = 1 - \frac{C_\mathrm{R}}{C_\mathrm{R}^0} \tag{2}$$

$$\eta_\mathrm{W} = \theta \times 100\% \tag{3}$$

where C_R and C_R^0 denote the corrosion rates of the samples, expressed in mg cm^{-2} h^{-1}, when exposed to the corrosive medium with and without the [C$_n$Py]Br inhibitor, respectively; m_1 and m_2 indicate the weights of the samples, prior to and following immersion, respectively, in mg; s denotes the sample's surface area, cm^2; t represents the duration of immersion, h; θ indicates the coverage rate, %; η_W signifies the corrosion inhibition efficiency, %.

2.5 Electrochemical measurements

Potentiodynamic polarization (PDP) and electrochemical impedance spectroscopy (EIS) tests were conducted in electrochemical workstation model CHI660E. Electrochemical measurements were performed with a three-electrode cell setup, comprising a working electrode (mild steel with an active area of 1 cm^2), a saturated calomel electrode as the reference, and a platinum electrode serving as the counter electrode. The temperature during the experiment was maintained at 298 K. Prior to each electrochemical impedance spectroscopy (EIS) measurement, the mild steel working electrode was submerged in the test solutions for 0.5 h to stabilize and achieve a steady-state open circuit potential (OCP).[3]

The EIS was conducted with an AC voltage amplitude of 10 mV and a frequency range of 100 kHz to 0.01 Hz. Eqn (4) was used to calculate the inhibition efficiency (η_E) using the charge transfer resistance found, R_ct.

$$\eta_\mathrm{E} = \frac{R_\mathrm{ct} - R_\mathrm{ct}^0}{R_\mathrm{ct}} \times 100\% \tag{4}$$

where R_ct^0 and R_ct represent the charge transfer resistance, respectively, in the presence and absence of different [C$_n$Py]Br inhibitor concentrations, Ω cm^2.

PDP investigations were carried out by scanning the potential within a range of ±250 mV relative to the open circuit potential (OCP) at a scan rate of 0.5 mV s^{-1}. The obtained corrosion current density I_corr was used to estimate the inhibition efficiency (η_P) by the formula (5).

$$\eta_\mathrm{P} = \frac{I_\mathrm{corr}^0 - I_\mathrm{corr}}{I_\mathrm{corr}^0} \times 100\% \tag{5}$$

where the current densities recorded with and without the [C$_n$Py]Br inhibitor are indicated by I_corr^0 and I_corr, respectively, and are expressed in μA cm^{-2}.

2.6 Surface analysis

The prepared metal specimens were immersed in a 1 M HCl solution with and without [C$_{12}$Py]Br inhibitor for 24 h at 298 K. Following the testing, the extracts were cleaned several times using both ethanol and acetone after first being rinsed with ionized water. Afterward, they were swiftly dried, sealed, and sent for further testing. To assess the extent of damage caused by corrosion and determine the elemental makeup of the products of corrosion on the surface, the EDS and SEM were utilized. XPS was conducted to characterize the properties and composition of the film formed on the mild steel surface.

2.7 Quantum chemical calculations

The efficiency of corrosion inhibitors can now be accurately predicted using quantum chemical calculations. In this study, a detailed analysis was performed to evaluate the influence of an aqueous solvent on quantum simulations, utilizing the DFT method at the B3LYP functional and the 6-31G(d,p) basis set. The COSMO model (H$_2$O, dielectric strength 78.54) has been added using the DMOL3 module of Materials Studio 2020 program.[2,27] The synthesized ionic liquids were optimized in their ground state, and frequency analyses were conducted.

This study analyzed the optimized molecular structure and evaluated several theoretical parameters. These parameters encompassed the highest occupied molecular orbital energy (E_HOMO), the lowest unoccupied molecular orbital energy (E_LUMO), the energy gap (ΔE_GAP), ionization potential (I), electron affinity (A), electronegativity (χ), hardness (η), softness (σ), and dipole moment (μ).[28] The electronic parameters were calculated using the DFT-Koopmans theorem, where $A = -E_\mathrm{LUMO}$ and $I = -E_\mathrm{HOMO}$. The formulas that followed were used to determine the remaining variables:

$$\Delta E = E_\mathrm{LUMO} - E_\mathrm{HOMO} \tag{6}$$

$$\chi = \frac{I + A}{2} \tag{7}$$

$$\eta = \frac{I - A}{2} \tag{8}$$

$$\sigma = \frac{2}{I - A} \tag{9}$$

$$\mu = \frac{I + A}{2} \tag{10}$$

The Pearson method formula is employed to determine the quantity of electrons exchanged:

$$\Delta N = \frac{\varphi_{\mathrm{Fe}} - \chi_{\mathrm{inh}}}{2(\eta_{\mathrm{Fe}} + \eta_{\mathrm{inh}})} \tag{11}$$

where χ_{inh} denotes the electronegativity of the inhibitor molecules, while η_{Fe} and η_{inh} represent the absolute hardness of iron and the inhibitor molecules, respectively. The theoretical value of η_{Fe} is 0 eV.

The DFT-derived values for the φ_{Fe} of Fe(100), Fe(110), and Fe(111) surfaces are 3.89, 4.82, and 3.78 eV, respectively. For this analysis, only the Fe(110) surface is considered, as it exhibits greater stability and a more densely packed structure.[29]

2.8 Molecular dynamics simulation

Molecular dynamics (MD) simulations are commonly applied and highly efficient methods used to investigate the interactions between inhibitors and metal surfaces. In this work, the Materials Studio 2020 programs, more especially the Forcite section, was used to examine the relationship between the molecule that inhibits and the Fe(110) the surface.[5,29] The Fe(110) surface was selected for this study because of its highly compact structure and lowest energy, which demonstrate its superior stability relative to other Fe surfaces, such as Fe(100) or Fe(111). The MD simulations were carried out under solvation conditions using 491H_2O, 9H_3O^+, 9Cl^-, and 1 optimized [C_nPy]Br molecule solution's composition. The simulation was conducted within a box with dimensions of 287 nm × 287 nm × 365 nm, it has an empty area of 190 nm and six Fe(110) levels with 12 × 12 Fe atoms per face. An Andersen thermostat operating in the 298–328 K spectrum of temperatures was used to run the simulation.[8,30] Following this, a 2000 ps simulation was carried out for the system under the *NVT* ensemble, using a time step of 1 fs. All calculations were performed under periodic boundary conditions, utilizing COMPASS II as the force field. The interaction energy ($E_{\mathrm{interaction}}$) between the inhibitor molecules and the Fe(110) surface was determined using eqn (12). The $E_{\mathrm{interaction}}$ is used to get the binding energy (E_{binding}) as shown in eqn (13) (ref. 31 and 32).

$$E_{\mathrm{interaction}} = E_{\mathrm{total}} - (E_{\mathrm{surface+solution}} + E_{\mathrm{inhibitor}}) \tag{12}$$

$$E_{\mathrm{binding}} = -E_{\mathrm{interaction}} \tag{13}$$

where the system's entire energy is denoted by E_{total}, the system's energy with no the inhibitor molecule by $E_{\mathrm{surface+solution}}$, and the system's power associated with the inhibitor molecule by $E_{\mathrm{inhibitor}}$.

3 Results and discussions

3.1 Weight-loss analysis

Although the mass loss method is a time-consuming approach for predicting corrosion rates and evaluating inhibition, it is a widely used direct technique for assessing general corrosion rates, especially in uniform corrosion conditions.[33] However, in practical situations, its reliability may vary depending on the specific corrosion mechanism. As observed from the Table 3, an increase in the concentration of corrosion inhibitor leads to a reduction in the corrosion rate and a corresponding increase in the inhibition rate. This implies that with an increased concentration of the inhibitor, larger inhibitor molecules were more effectively adsorbed onto the mild steel surface, resulting in the formation of a protective film. Therefore, the creation of a barrier film by the inhibitor hinders the penetration of the corrosive agent, preventing it from reaching the metal surface.[34]

3.1.1 Effect of inhibitor concentration. The corrosion inhibition efficiency of [C_nPy]Br ILs increases with concentration up to 2 mmol L^{-1}, beyond which further improvement becomes marginal (Fig. 3 and Table 3). This saturation behavior suggests limited availability of adsorption sites on the mild steel surface at higher concentrations.

3.1.2 Effect of alkyl chain length. At equivalent concentrations, [C_{12}Py]Br exhibits the highest inhibition efficiency, followed by [C_8Py]Br and [C_4Py]Br. The superior performance of [C_{12}Py]Br is attributed to its longer alkyl chain, which promotes the formation of a denser hydrophobic layer and broader surface coverage, thereby enhancing the physical barrier effect against corrosive agents.[35]

Based on these results, 2 mmol L^{-1} was selected as the optimal concentration for subsequent studies, balancing inhibition efficacy and practical applicability.

Temperature plays a crucial role in affecting the corrosion process of metals. As shown in Fig. 4 and Table 4, four different temperature ranges were investigated. A detailed analysis shows that as the temperature rises, there is a gradual reduction in inhibition efficiency. This phenomenon can be attributed to the fact that elevated temperatures increase the average kinetic energy of the reacting molecules, leading to the desorption of inhibitor molecules from the surface of mild steel.[36,37]

Table 3 Corrosion rate and the inhibition efficiency for mild steel immersed in 1 M HCl in the absence and presence of [C_nPy]Br inhibitors at 298 K

Inhibitor	Conc. (mmol L^{-1})	C_R (mg cm^{-2} h^{-1})	η_w (%)
Blank	—	0.681	—
[C_4Py]Br	0.25	0.360	47.2
	0.5	0.320	53.1
	1	0.266	60.9
	2	0.202	70.3
	4	0.198	70.9
	8	0.197	71.1
[C_8Py]Br	0.25	0.269	60.5
	0.5	0.233	65.8
	1	0.193	71.6
	2	0.146	78.5
	4	0.141	79.3
	8	0.133	80.4
[C_{12}Py]Br	0.25	0.193	71.6
	0.5	0.160	76.5
	1	0.133	80.4
	2	0.080	88.3
	4	0.060	91.2
	8	0.046	93.2

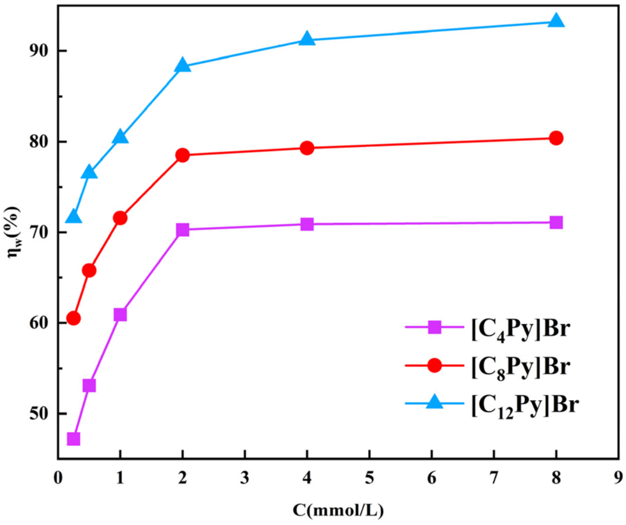

Fig. 3 Corrosion inhibition of different concentrations of $[C_nPy]Br$ IL at 298 K.

3.2 Electrochemical measurements

3.2.1 Tafel polarization measurements. A polarization study was conducted to gain a deeper understanding of the reaction dynamics at both the anode and cathode during the corrosion process. The mild steel polarization curves at 298 K in a 1 M HCl solution, both with and without varying $[C_nPy]Br$ inhibitor concentrations, are shown in Fig. 5. Table 5 presents the electrochemical parameters obtained from the measurements, which include the anodic Tafel slope (β_a), cathodic Tafel slope (β_c), corrosion current density (I_{corr}), and corrosion potential (E_{corr}).

The anodic Tafel slope (β_a) and cathodic Tafel slope ($-\beta_c$) are sensitive indicators of the inhibition degree of anodic dissolution and cathodic hydrogen evolution reactions, respectively.

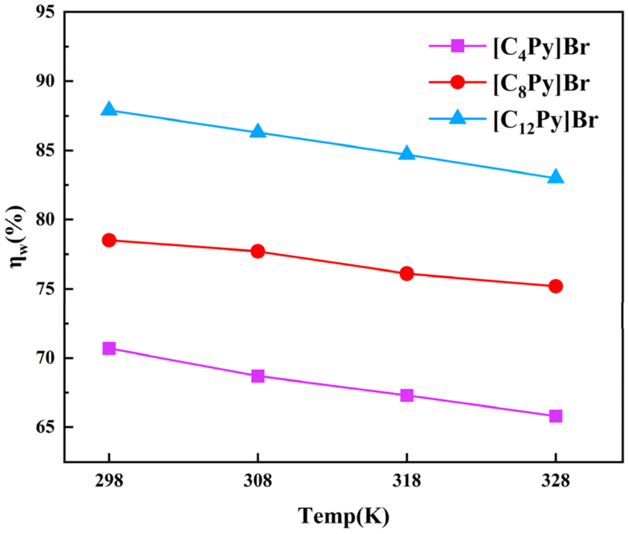

Fig. 4 Corrosion inhibition of 2 mmol $[C_nPy]Br$ IL at different temperatures.

Table 4 Presents the corrosion rate and inhibition efficiency of mild steel in 1 M HCl with $[C_nPy]Br$ inhibitor concentrations of 0 and 2 mmol at various temperatures

Inhibitor	Temp (°C)	Temp (K)	C_R (mg cm^{-2} h^{-1})	η_w (%)
Blank	25	298	0.681	—
	35	308	0.735	
	45	318	0.793	
	55	328	0.868	
$[C_4Py]Br$	25	298	0.202	70.7
	35	308	0.213	68.7
	45	318	0.222	67.3
	55	328	0.233	65.8
$[C_8Py]Br$	25	298	0.146	78.5
	35	308	0.152	77.7
	45	318	0.162	76.1
	55	328	0.169	75.2
$[C_{12}Py]Br$	25	298	0.082	87.9
	35	308	0.093	86.3
	45	318	0.104	84.7
	55	328	0.116	83.0

For $[C_nPy]Br$ inhibitors, we observed that: for anodic reactions, the β_a value decreases with the increase of inhibitor concentration(*e.g.*, for $[C_{12}Py]Br$, β_a decreased from 13.694 V dec^{-1} in the blank to 7.854 V dec^{-1} at 8 mmol L^{-1}), indicating a moderate suppression of Fe oxidation (anodic dissolution). For cathodic reactions, the $-\beta_c$ values decreased slightly (*e.g.*, for $[C_{12}Py]Br$, $-\beta_c$ decreased from 7.441 V dec^{-1} in the blank to 6.138 V dec^{-1} at 8 mmol L^{-1}), suggesting a stronger inhibition of the cathodic hydrogen evolution reaction ($2H^+ + 2e^- \rightarrow H_2$). This indicates that longer alkyl chains amplify this differential inhibition. $[C_{12}Py]Br$ showed a more pronounced decrease in $-\beta_c$ (18.8% reduction compared to the blank) than the change in β_a (42.7% reduction), indicating that the longer hydrophobic alkyl chain preferentially hinders the diffusion of H^+ to the metal surface (cathodic reaction) by forming a denser protective film, while still suppressing anodic dissolution through adsorption on active Fe sites. This differential inhibition confirms that $[C_nPy]Br$ acts as a mixed-type inhibitor with a slight preference for cathodic inhibition. The pyridinium ring adsorbs on Fe active sites to suppress anodic dissolution *via* coordinate bonds, while the alkyl chain forms a hydrophobic barrier that more effectively blocks H^+ transport to the cathode, leading to stronger cathodic inhibition.

As seen in Fig. 5, in the presence of inhibitors, the curves of polarization exhibit a shift in the E_corr values, either to more anodic or cathodic orientations, relative to the blank solution. As the concentration of $[C_nPy]Br$ ILs increases, irregular variations in the E_{corr} values are observed. This indicates that the inhibitors under investigation influence both the anodic and cathodic reactions.[29]

When a compound's change in E_{corr} is less than 85 mV, it is typically regarded as a mixed-type inhibitor. On the other hand, if the shift in E_{corr} surpasses 85 mV relative to the E_{corr} of the uninhibited solution, the corrosion type will be categorized as either anodic or cathodic. In this research, the E_{corr} values for the three ILs at varying concentrations are all below 85 mV,

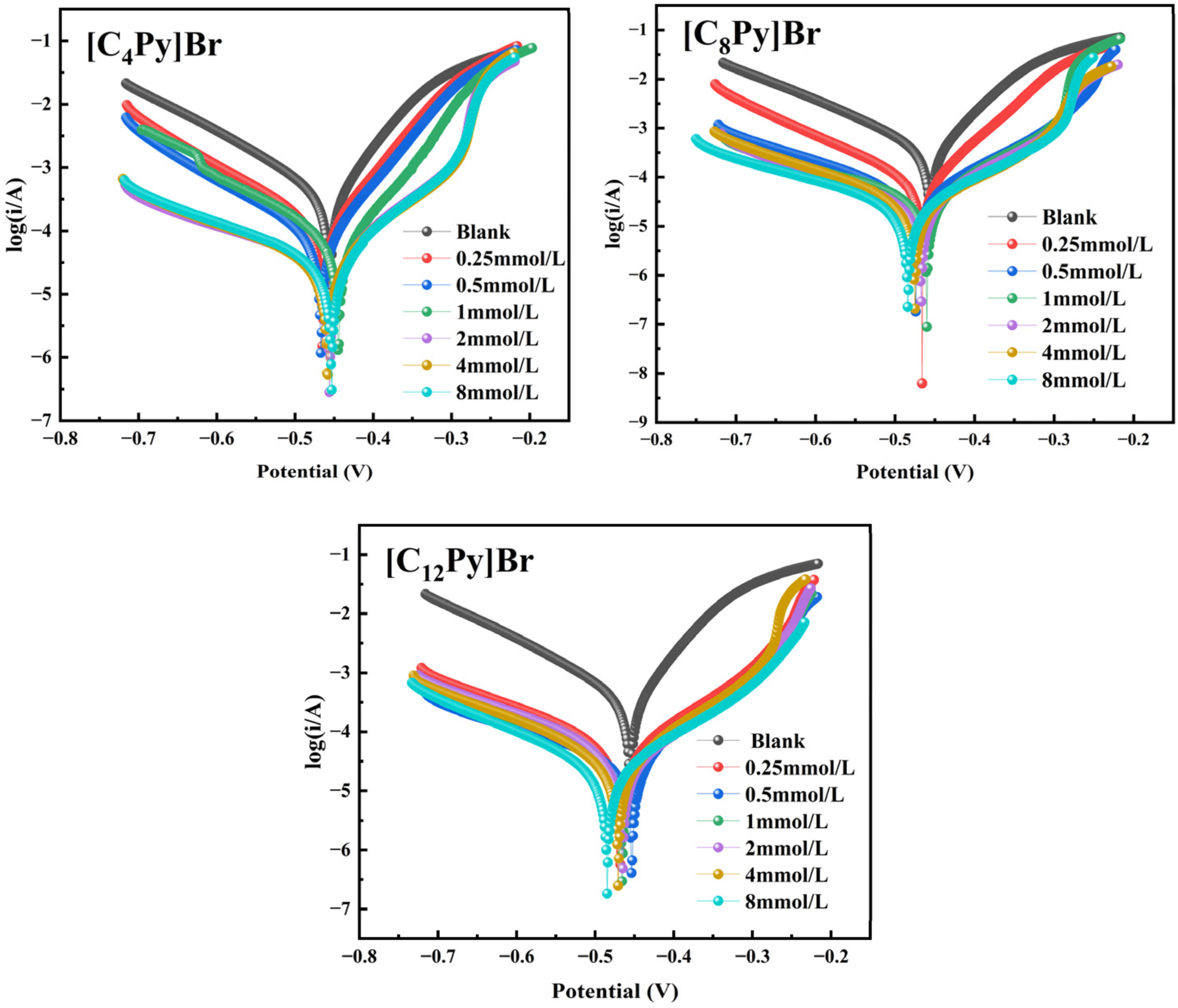

Fig. 5 Tafel curves for mild steel in 1 M HCl solution containing without and with different concentrations of [C_nPy]Br ILs at 298 K.

suggesting that these ILs fall under the mixed-type inhibitor category.[38,39]

Table 5 unequivocally demonstrates that I_{corr} is significantly reduced when [C_nPy]Br inhibitors are present. The values of I_{corr} decreased from 373.8 μA cm^{-2} in the blank solution to 35.84 μA per cm^2 ([C_4Py]Br), 26.72 μA per cm^2 ([C_8Py]Br), and 22.14 μA per cm^2 ([C_{12}Py]Br) at a concentration of 8 mmol L^{-1}, the corresponding η_p reached 90.4%, 92.9%, and 94.1%. Because of the increased adsorption of [C_nPy]Br ILs molecules onto the active sites at the mild steel/solution interface as the amount of the inhibitor increases, there is a positive correlation between the concentration of added inhibitors and the η_p.[36] Under identical concentration conditions, the inhibitory effectiveness escalates as the length of the cationic alkyl chain extends, corroborating the findings from weight loss assays. [C_nPy]Br ILs efficiently inhibit both cathodic and anodic corrosion reactions, as seen by Table 5, which shows variations in the β_a and $-\beta_c$ values with the introduction of inhibitors.

3.2.2 Electrochemical impedance spectroscopy (EIS). An effective method for examining the causes of corrosion at the metal-solution interface is electrochemical impedance spectroscopy. Fig. 6 and 7 show the Nyquist and Bode plots of mild steel in 1 M HCl solution at 298 K with and without varying [C_nPy]Br concentrations.

The Nyquist plots (Fig. 6) distinctly show a flattened capacitive loop, suggesting that the corrosion mechanism is mainly controlled by the charge transfer at the interface between the mild steel surface and the solution. The imperfect semicircular shape of the capacitive loops is usually ascribed to frequency dispersion brought on by the mild steel's surface roughness and heterogeneity. The Nyquist diagrams display irregular semicircles, suggesting that a simple capacitance model, such as C_{dl}, is not suitable for direct calculations. Consequently, a constant phase element (CPE$_{dl}$) is added to the circuit in its place.[40] However, the similarity in the shapes of the curves for all tested inhibitors implies that the dissolution mechanism remains

Table 5 PDP parameters for mild steel at 298 K in 1 M HCl solution in the absence and presence of different concentrations of $[C_nPy]Br$ ILs

Inhibitor	Conc. (mmol L^{-1})	E_{corr} (V)	I_{corr} ($\mu A\ cm^{-2}$)	β_a (V dec^{-1})	$-\beta_c$ (V dec^{-1})	η_p (%)
Blank	—	−0.455	373.8	13.694	7.441	—
$[C_4Py]Br$	0.25	−0.465	111.8	15.206	7.024	70.1
	0.5	−0.467	74.26	14.989	6.793	80.1
	1	−0.445	60.59	15.359	6.522	83.8
	2	−0.456	39.15	9.218	4.333	89.5
	4	−0.458	36.64	8.869	4.791	90.2
	8	−0.453	35.84	9.402	4.728	90.4
$[C_8Py]Br$	0.25	−0.466	75.15	14.077	7.302	79.9
	0.5	−0.474	45.69	8.357	5.916	87.8
	1	−0.460	43.4	8.814	4.519	88.4
	2	−0.467	33.48	8.498	5.214	91.0
	4	−0.475	29.43	8.003	5.888	92.1
	8	−0.484	26.72	7.739	5.079	92.9
$[C_{12}Py]Br$	0.25	−0.468	51.49	8.504	5.827	86.2
	0.5	−0.454	38.72	8.273	4.641	89.6
	1	−0.466	32.72	8.635	5.101	91.2
	2	−0.465	28.5	8.476	5.861	92.4
	4	−0.471	26.18	8.689	6.287	93.0
	8	−0.485	22.14	7.854	6.138	94.1

consistent, regardless of the presence or absence of $[C_nPy]Br$ ILs. The diameter of the capacitive loops is considerably increased by the inclusion of the synthesized ILs in comparison to the blank solution, as shown in Fig. 6, and the loop diameter increases as the inhibitor concentration increases. The diameter grows greater as the length of the cation chain increases at every concentration level.[37] The increasing diameter of the capacitive loops indicates a rise in charge transfer resistance (R_{ct}), which suggests that the inhibitor is effectively hindering the electron transfer between the metal surface and the corrosive medium. This behavior reflects the formation of a more stable and compact protective layer on the steel surface, thereby enhancing corrosion resistance. Such an increase in R_{ct} is commonly associated with improved surface coverage and stronger adsorption of the inhibitor molecules.

As shown in Fig. 7, the phase angle observed for the blank medium was noticeably lower when compared to the values at different inhibitor concentrations. The incorporation of $[C_nPy]Br$ ILs resulted in elevated phase angle values, signifying an enhanced capacitive nature and diminished surface deterioration. This suggests that a protective layer has developed at the metal-solution contact.[41,42] The $|Z|$ value at low frequencies increases progressively with the rise in inhibitor concentration. This is explained by the improved resistance to polarization across the metal/solution interaction. Moreover, this leads to a reduction in the roughness of the metal surface. This further supports the idea that the $[C_nPy]Br$ ILs adsorb onto the surface. The impedance plot indicates that the system exhibits a single time constant. From the previous analysis, the experimental data can be fitted using a Randles equivalent circuit (Fig. 8), as illustrated in Fig. 7.[30] Electrolyte resistance (R_s), charge transfer resistance (R_{ct}), and CPE_{dl} are the components of the circuit diagram, respectively. An accurate fit was obtained by analyzing the impedance using the CPE_{dl}.[43,44] The following formula is used to determine the capacitance of both layers at the metal/solution interface:

$$C_{dl} = T^{(1/n)} \times R_s^{(1-n)n} \tag{14}$$

The following formula is used to determine the impedance related to the constant phase element (CPE_{dl}):

$$Z_{CPE} = \frac{1}{T(j\omega)^n} \tag{15}$$

where n denotes the extent to which the element departs from exhibiting pure capacitive. The CPE_{dl} acts like a pure capacitance when ($n = 1$). On the other hand, the CPE_{dl} represents inductance or pure resistance, respectively, when $n = -1$ or 0. According to Table 1, the value of n varies between 0.780 and 0.934, indicating a minor deviation between the ideal and actual capacitance.[26,45]

The parameters obtained through fitting with ZView software are presented in Table 6. As the dosage of corrosion inhibitors increases, the values of C_{dl} exhibit a consistent decrease. According to the Helmholtz model, this behavior can be explained by either a rise in the electric double layer's thickness or a decrease in local permittivity. This suggests that corrosion inhibitor molecules adsorb onto the metal surface, displacing the previously adsorbed water molecules or chloride ions.[46] The results from the kinetic potential polarization method and the EIS measurements show a high degree of consistency in the fitting data. This demonstrates that mild steel can be effectively protected against corrosion by $[C_nPy]Br$ ILs in 1 M HCl.[28]

3.3 Adsorption isotherm

The inhibitor-metal surface interaction was investigated using the adsorption isotherm. When the expression (16) is used, the coefficient value approaches 1, indicating that the Langmuir adsorption isotherm is a useful tool for examining the inhibitor's process of adsorption.[47] A variety of adsorption isotherms,

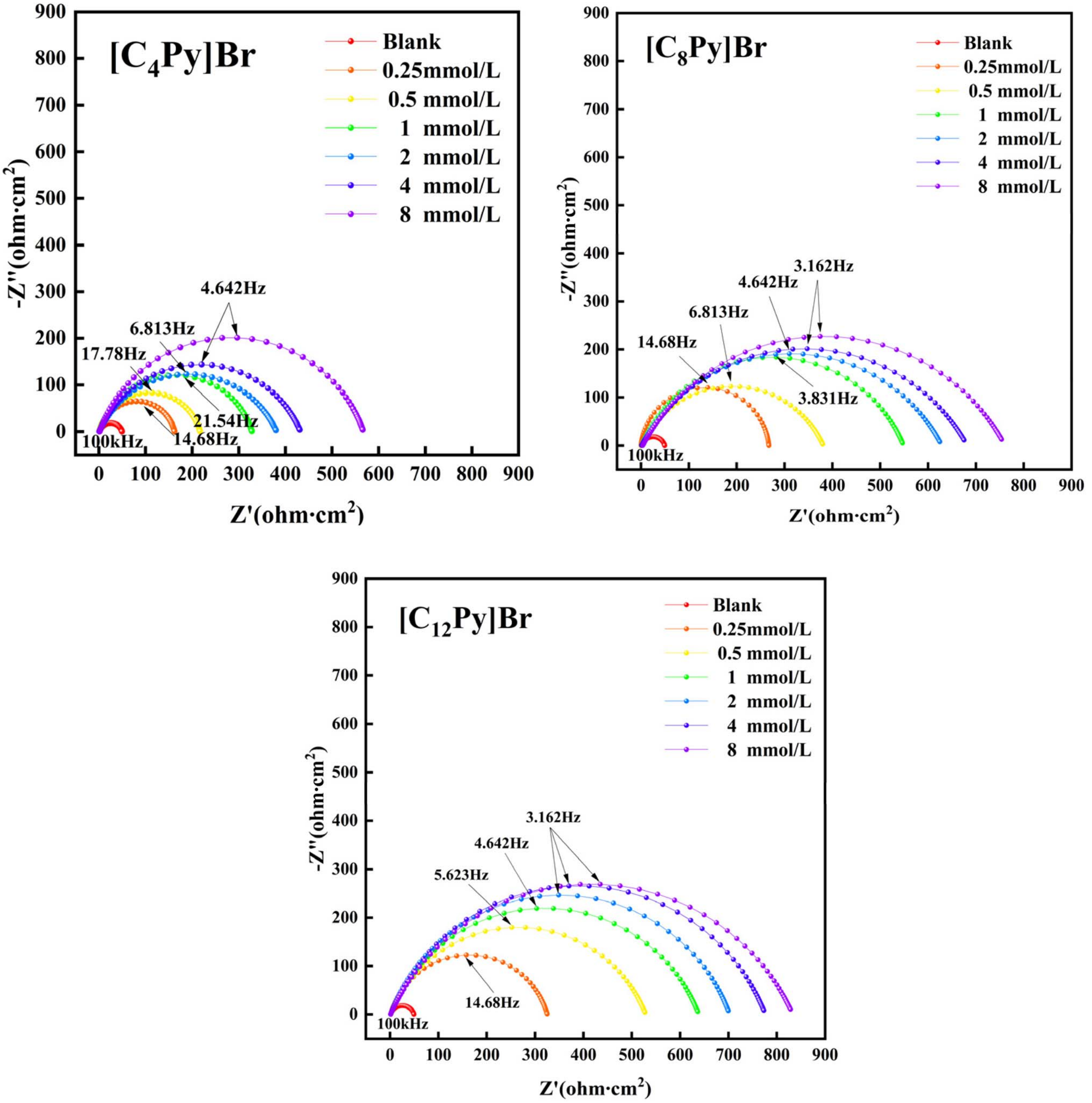

Fig. 6 The Nyquist plots were recorded at 298 K for metal specimens in 1 M HCl with and without different doses of $[C_nPy]Br$ inhibitor.

including Temkin and Frumkin, have been assessed. However, the Langmuir adsorption isotherm provided the most accurate fit. Fig. 9 represents the adsorption isotherm plots for various concentrations. Corresponding parameters are presented in Table 7.

$$\frac{C_{\text{inh}}}{\theta} = \frac{1}{K_{\text{ads}}} + C_{\text{inh}} \tag{16}$$

where C_{inh}, K_{ads} and θ stand for the inhibitor's concentration, the adsorption equilibrium constant, and the surface coverage ratio. Eqn (17) was used to get the Gibb's free energy (ΔG_{ads}) from the Langmuir isotherm parameters.

$$\Delta G_{\text{ads}} = -RT\ln(55.5K_{\text{ads}}) \tag{17}$$

The mole fraction of H_2O in solution is 55.5, the absolute temperature is T, and the universal gas constant is R (8.314 J (mol K)$^{-1}$).[48]

The three ILs under investigation have a considerable potential to adsorb on the metal-electrolyte interfaces, as shown by the comparatively high K_{ads} values in Table 7.[21] Additionally, when the alkyl chains length on the cation increases, the K_{ads} values increase as well. The powerful connection between corrosion inhibitor molecules and the metal surface, as well as the spontaneous nature of adsorption, are highlighted by the

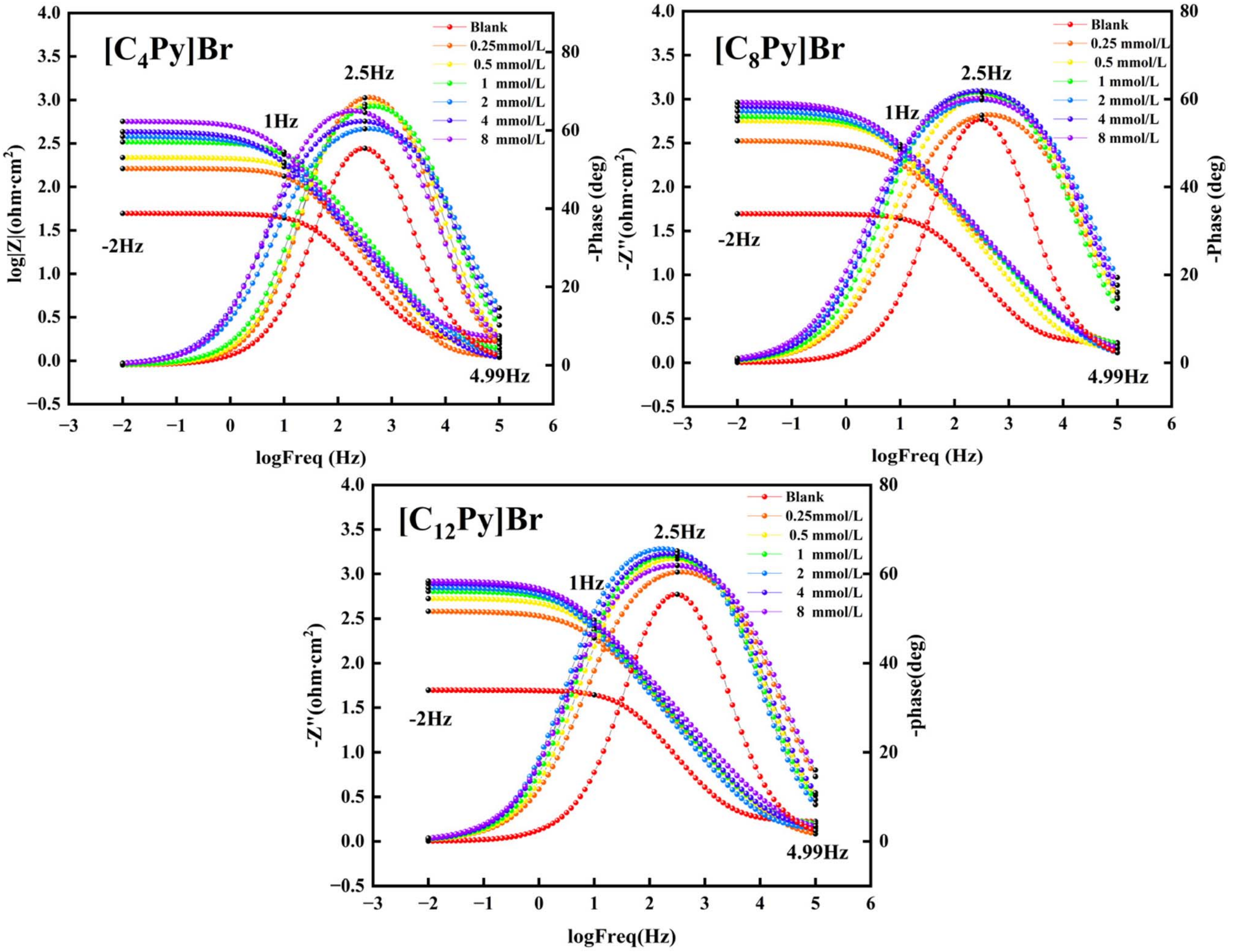

Fig. 7 Bode graphs of metal samples at 298 K in 1 M HCl with and without varying [C$_n$Py]Br inhibitor.

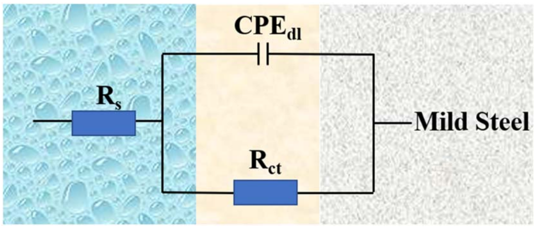

Fig. 8 Equivalent circuit used to fit the corrosion impedance spectrum of mild steel.

negative ΔG_{ads} values, which reveal a thermodynamically advantageous process. According to previous research, it is understood that when the ΔG_{ads} value reaches -20 kJ mol^{-1}, the inhibitor's adsorption is classified as physisorption. Conversely, when the ΔG_{ads} value exceeds -40 kJ mol^{-1}, the adsorption process is considered chemisorption. In this research, the ΔG_{ads} values of three studied ILs fall within the range of -34 to -36 kJ mol^{-1}, substantiating that [C$_n$Py]Br would adsorb on the metal surface by both physisorption and chemisorption. Thus, in a 1 M HCl solution, [C$_n$Py]Br exhibits a mixed adsorption behavior on the metal surface.[49]

3.4 SEM-EDS studies

The mild steel surface was examined using SEM and EDS to evaluate its composition and morphology. The findings are shown in Fig. 10(a–f). Prior to exposure to corrosive environments, Fig. 10(a) shows a smooth surface of the polished sample. Nevertheless, after immersion in the acidic solution, the mild steel specimen (Fig. 10(b)) showed significant corrosion damage, resulting in a rough and irregular surface texture. After the introduction of 2 mmol of [C$_{12}$Py]Br, a distinct change in the surface morphology was observed (Fig. 10(c)).[8,30] Because of the protective film that formed, the surface showed less roughness. This result suggests that [C$_{12}$Py]Br successfully formed a protective layer, avoiding direct contact between the aggressive solution and the mild steel surface. In Fig. 10(d–f), the elemental composition analysis of the mild steel surface submerged in an HCl solution, both with and without the optimal concentration of [C$_{12}$Py]Br, is shown. The polished mild steel surface (Fig. 10(d)) displayed a prominent iron peak along

Table 6 Zview-fitted electrochemical impedance parameters

Inhibitor	Conc. (mmol L^{-1})	R_s (Ω cm^2)	n	R_{ct} (Ω cm^2)	C_{dl} (μF cm^{-2})	$\chi^2 \times 10^{-3}$	η_E (%)
Blank	—	1.659	0.827	48.04	42.3	0.44	—
[C_4Py]Br	0.25	1.500	0.861	161.2	22.1	0.56	70.2
	0.5	1.440	0.844	216.1	16.2	1.10	77.8
	1	1.308	0.851	327.2	15.2	1.34	85.3
	2	1.119	0.844	367	11.6	1.45	86.9
	4	0.969	0.847	431.6	9.98	0.76	88.9
	8	0.954	0.849	595.3	8.51	0.66	91.9
[C_8Py]Br	0.25	1.484	0.934	267.3	44.7	0.36	82.0
	0.5	1.235	0.811	380.2	25.1	0.80	87.4
	1	1.158	0.802	547.3	19.3	0.48	91.2
	2	1.078	0.816	627.8	16.8	0.33	92.4
	4	1.077	0.780	680.5	13.4	0.53	92.9
	8	0.942	0.838	757.3	7.6	0.32	93.7
[C_{12}Py]Br	0.25	1.404	0.846	324	36.4	0.23	85.2
	0.5	1.334	0.833	527.7	23.7	0.65	90.9
	1	1.277	0.808	637.3	15.9	0.89	92.5
	2	1.203	0.789	719.8	13.7	1.46	93.3
	4	1.183	0.790	761.9	12.8	0.93	93.7
	8	1.142	0.792	832.1	12.5	0.75	94.2

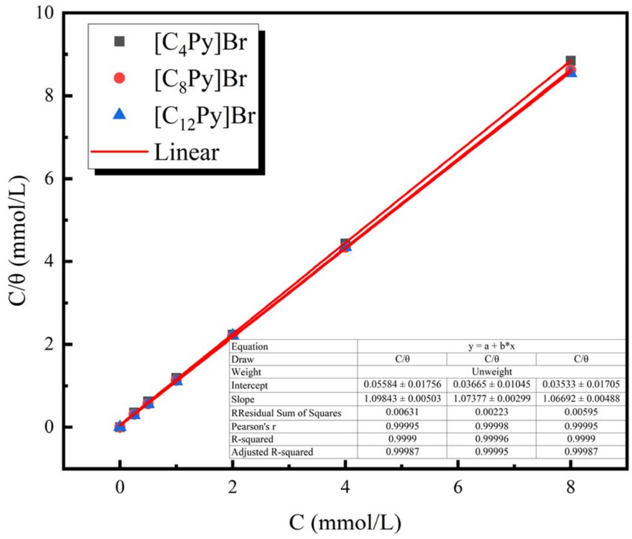

Equation	y = a + b*x		
Draw	C/θ	C/θ	C/θ
Weight	Unweight		
Intercept	0.05584 ± 0.01756	0.03665 ± 0.01045	0.03533 ± 0.01705
Slope	1.09843 ± 0.00503	1.07377 ± 0.00299	1.06692 ± 0.00488
RResidual Sum of Squares	0.00631	0.00223	0.00595
Pearson's r	0.99995	0.99998	0.99995
R-squared	0.9999	0.99996	0.9999
Adjusted R-squared	0.99987	0.99995	0.99987

Fig. 9 Langmuir adsorption plot of [C_nPy]Br ILs for mild steel in 1 M HCl.

with other characteristic elements typical of mild steel. Nevertheless, the Fe peak was significantly diminished when exposed to the uncontrolled acidic solution (Fig. 10(e)), leading to a considerable decrease in the Fe content from 96.21% to 78.40%. The oxygen (O) peak in the EDS spectrum of mild steel specimen soaked in acid solution significantly increased, while a new choline (Cl) peak appeared.[38,50] This indicates that the acidic exposure led to the formation of complex hydroxides, oxides, and chlorides on the surface of the mild steel. Following the addition of [C_{12}Py]Br, the strength of the iron peak improved to 95.82% (Fig. 10(f)), suggesting a decrease in acidic corrosion.[51]

Table 7 Thermodynamic parameters associated with different adsorption curves

Inhibitor	R^2	Slope	K_{ads}	ΔG_{ads} (kJ mol^{-1})
[C_4Py]Br	0.99987	1.098	17 908.309	−34.213
[C_8Py]Br	0.99995	1.073	27 285.130	−35.257
[C_{12}Py]Br	0.99987	1.066	28 304.557	−35.348

3.5 XPS analysis

XPS research was used to examine the interaction between the corrosion inhibitor and the surface of the metal, offering crucial information about the electronic condition and chemical makeup of the metal's outermost layers.[51] Fig. 11(a–d) shows the XPS survey plots and the high-resolution spectra that correspond to them.

The conventional peaks of Fe, O, and C are shown in Fig. 11(a), which is clearly caused by the process of adsorption of the [C_{12}Py]Br inhibitor. The C 1s spectra are shown in Fig. 11(b), with three deconvoluted peaks at 284.8 eV, 286.4 eV, and 288.6 eV. The initial peak, observed around 284.8 eV, corresponds to the C–H and C–C bonds. The peak at 286.4 eV (C–N bonds) directly indicates interactions between the pyridinium ring of [C_{12}Py]Br and the Fe surface. This bond forms *via* electron donation from the pyridinium N atom to Fe's empty d-orbitals, providing critical evidence for chemical adsorption—consistent with quantum chemical calculations showing high electron density on the pyridinium ring (Section 3.6). Though the N 1s signal is undetectable (due to low surface coverage), the C–N bond in C 1s spectra confirms the pyridinium ring's involvement in surface binding. Meanwhile, the second peak, appearing at 286.4 eV, is attributed to either C–O or C–N bonds. The final fitted peak, positioned near 288.6 eV, is characterized by a high binding energy and is likely associated

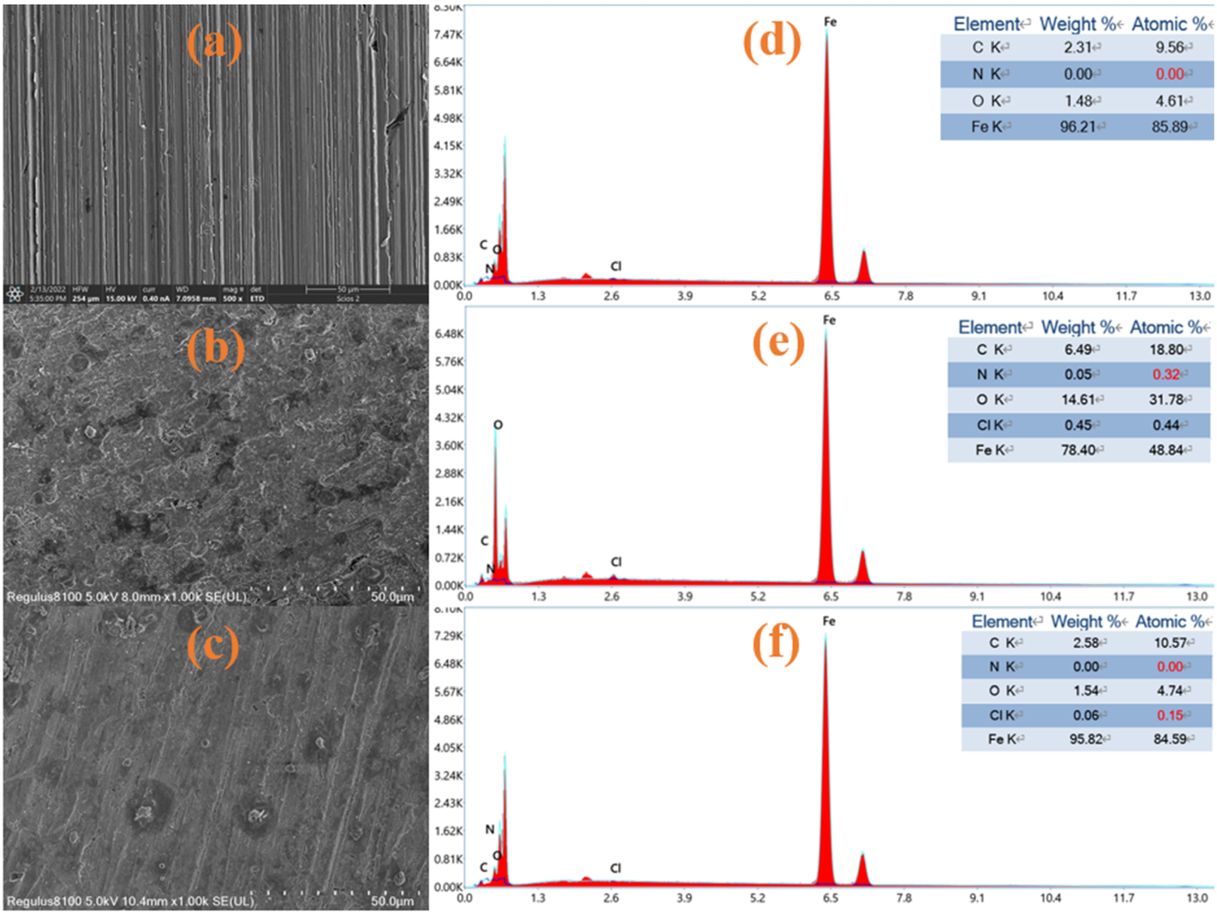

Fig. 10 SEM images and corresponding EDS spectra are shown for (a and d) mild steel prior immersion in HCl, (b and e) after 24 h of immersion in HCl without the inhibitor, (c and f) with $[C_{12}Py]Br$.

with the C=O group.[52] As shown in Fig. 11(c), the peak of O 1s spectrum is also fitted into three peaks. The three fitted peaks are 530.1 eV, 531.9 eV, and 532.1 eV, respectively. The initial peak is assigned to O^{2-}, theoretically linked to the bond between Fe^{3+} and Fe_2O_3. Meanwhile, the second peak corresponds to OH^-, indicative of its presence in hydrous iron oxides such as FeOOH. The final peak is likely associated with the oxygen in adsorbed H_2O molecules. For the Fe 2p spectra (Fig. 11(d)), the peaks at 711.2 eV and 713.8 eV are attributed to ferric compounds such as Fe_2O_3 and FeOOH, respectively.[53] The peak at 716.2 eV associated with the satellite of Fe(III) and the peak at 725 eV is attributed to the presence of various iron species, including Fe_3O_4, α-F_2O_3, and FeOOH. Based on XPS analysis, it is evident that $[C_{12}Py]Br$ molecules undergo chemisorption onto the mild steel surface, a finding that aligns with the conclusions drawn from the thermodynamic study. Consequently, in acidic conditions, $[C_nPy]Br$ ILs demonstrate exceptional effectiveness as mild-steel inhibitors of corrosion.[51]

3.6 Quantum chemical calculations

Quantum chemical simulations were utilized to further investigate how the molecular structure of $[C_nPy]Br$ relates to its effectiveness in corrosion inhibition.

Based on frontier orbital theory, the HOMO (highest occupied molecular orbital) and LUMO (lowest unoccupied molecular orbital) provide insights into potential adsorption sites for inhibitor molecules and help forecast the strength and stability of their interactions with metal surfaces.[54,55] In general, the E_{HOMO} indicates an inhibitor's ability to transfer electrons to the metal surface, while the E_{LUMO} reflects the inhibitor's tendency to accept electrons from the metal. The energy gap (ΔE) was shown to correspond with the rate of corrosion. As ΔE increases, molecular stability improves, reducing the likelihood of adsorption. Conversely, reduced stability often improves the capacity of molecules to adhere to metal surfaces, effectively preventing corrosion. Table 8 shows the calculated quantum chemical descriptors. The results reveal that the energy gap follows this sequence: $[C_{12}Py]Br < [C_8Py]Br < [C_4Py]Br$. This configuration indicates that $[C_{12}Py]Br$ is expected to show higher reactivity toward the metal surface, resulting in improved corrosion inhibition, which corresponds well with the experimentally observed trend in efficiency.[56] Fig. 12 illustrates the optimized geometries, frontier molecular orbital distributions, and molecular electrostatic potential maps of the $[C_nPy]Br$ ionic liquids. The findings from Fig. 12 reveal that the HOMO orbitals are primarily localized near the anions, enabling these

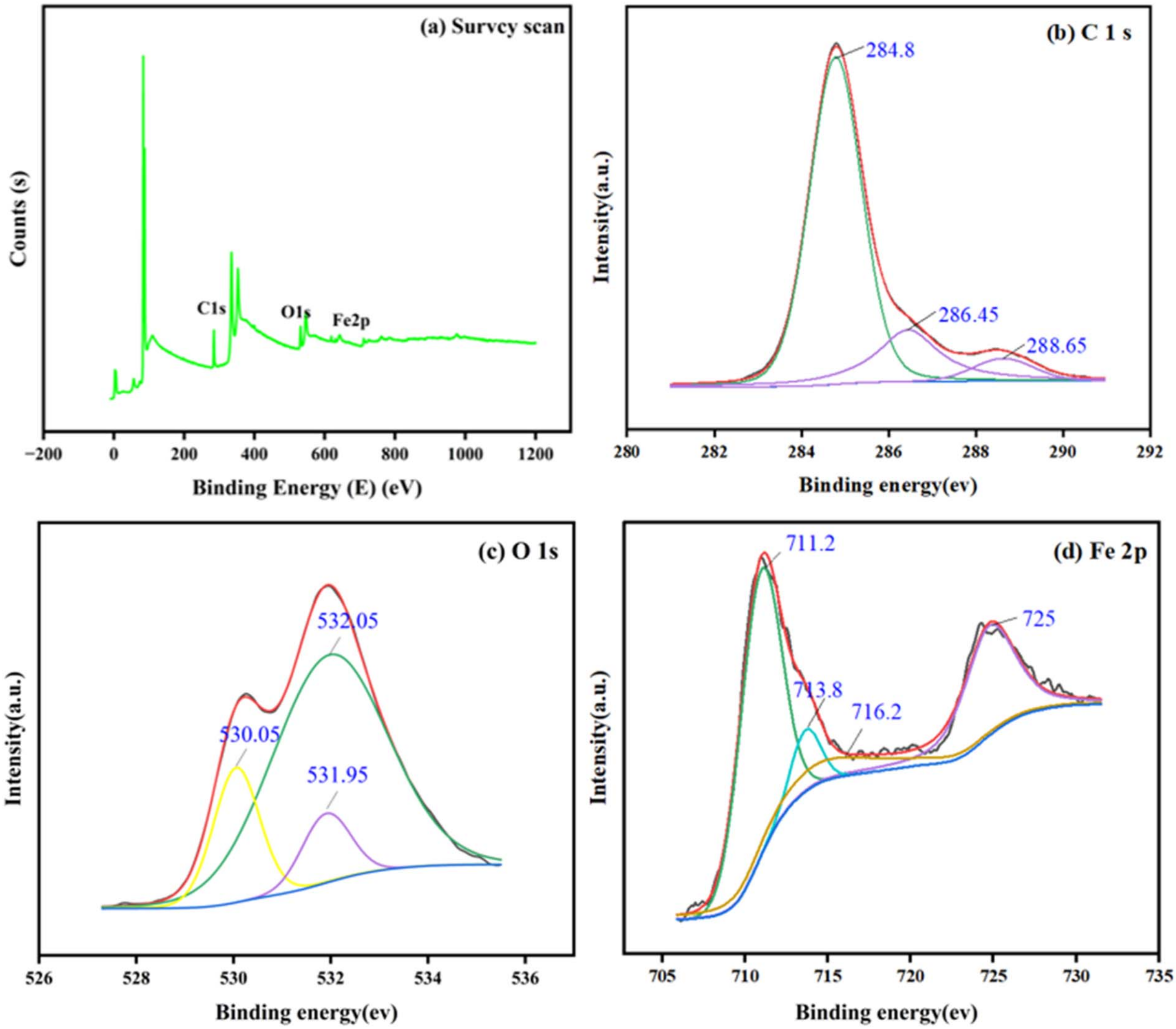

Fig. 11 XPS spectra of mild steel surface in presence of $[C_{12}Py]Br$: (a) full scanned spectrum; (b) C 1s; (c) O 1s; (d) Fe 2p.

regions to donate electrons to the metal surface and establish coordination bonds. Specifically, the HOMO is concentrated on the pyridinium ring (especially the N atom and adjacent C atoms), confirming this ring as the key electron-donating site for coordination with Fe. The MEP map (Fig. 12) further shows negative electrostatic potential on Br^-, which facilitates its pre-adsorption on the positively charged Fe surface *via* electrostatic interactions—explaining why Br^- enhances $[C_nPy]^+$ adsorption (supported by EIS data in Table 6 showing reduced Cdl with increasing $[C_nPy]Br$ concentration). These results clarify that both the pyridinium ring (chemical adsorption) and Br^- (electrostatic attraction) are indispensable functional groups. The LUMO orbitals are mainly located around the cationic ring structure, which may serve as acceptors for electrons on the metal surface, forming feedback bonds. These regions correspond to the active sites of the corrosion inhibitors being studied.

The calculations show that $[C_{12}Py]Br$ exhibits the lowest hardness values compared to $[C_4Py]Br$ and $[C_8Py]Br$. It was observed that the inhibitor exhibiting the lowest global

Table 8 $[C_nPy]Br$ ILs' quantum chemical characteristics (E_{HOMO}: highest occupied molecular orbital energy, E_{LUMO}: lowest unoccupied molecular orbital energy, ΔE: energy gap, I: ionization potential, A: electron affinity energy, μ: dipole moment, χ: electronegativity, η: hardness, σ: softness, ΔN: number of electrons transferred)

Inhibitor	E_{HOMO} (eV)	E_{LUMO} (eV)	ΔE (eV)	I (eV)	A (eV)	μ (D)	χ (eV)	η (eV)	σ (eV)	ΔN (eV)
$[C_4Py]Br$	−6.275	−2.356	3.919	6.275	2.356	−4.315	4.315	1.959	0.510	0.129
$[C_8Py]Br$	−6.270	−2.353	3.916	6.270	2.354	−4.312	4.312	1.952	0.519	0.130
$[C_{12}Py]Br$	−6.268	−2.351	3.915	6.268	2.353	−4.311	4.311	1.941	0.537	0.130

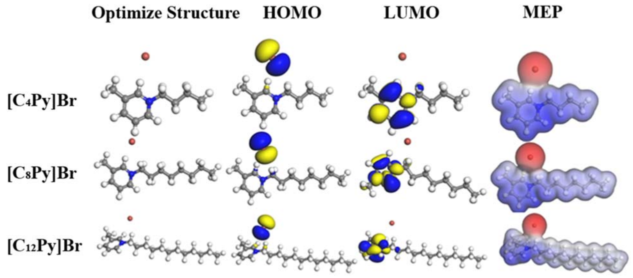

Fig. 12 Optimized structures, HOMO orbitals, LUMO orbitals, and MEP maps for [C_nPy]Br.

hardness (and consequently the highest global softness) is anticipated to demonstrate the greatest inhibition efficiency. Our findings reveal that [C_{12}Py]Br, characterized by the highest softness value (0.537 eV), achieves the most effective inhibition performance. In contrast, [C_4Py]Br, with the lowest softness value (0.510 eV), exhibits relatively weaker inhibition efficiency, as shown in Table 8.

Electronegativity (χ) is a crucial parameter to consider when comparing corrosion inhibitors with similar molecular structures. As per Pearson's theory, when two systems interact, electrons will flow from an area of higher chemical potential to one of lower potential. This process continues until equilibrium is achieved in the chemical potential. The work function for Fe(110) (4.8 eV) is greater than the electronegativity of all three [C_nPy]Br molecules. Consequently, the [C_nPy]Br molecules primarily adsorb onto the Fe(110) surface, facilitated by electron transfer from a metal orbital to an available free orbital. The electronegativity values of the molecules examined exhibit the trend [C_{12}Py]Br < [C_8Py]Br < [C_4Py]Br, which aligns with the sequence of inhibitory effectiveness observed in the electrochemical experiments.[28]

The stability and reactivity of corrosion inhibitor molecules are largely determined by the rate of electron transfer (ΔN). Theoretically, the corrosion inhibitor molecules have a stronger internal affinity when the computed value of ΔN is greater than 0. Consequently, these molecules' electrons are moved to the metal atoms, exhibiting improved inhibitory qualities. The corrosion inhibitor molecules have enough electron-donating capacity to successfully stop mild steel from corroding if ΔN is less than 3.6.[57,58] As presented in Table 8, the calculated values of ΔN for the [C_nPy]Br molecules investigated in this study are all above zero but do not exceed 3.6. This indicates that the Fe atom's unoccupied d orbitals can receive electron donations from the [C_nPy]Br molecules.

The molecular electrostatic potential (ESP), which provides a fundamental representation of a molecule's electronic structure, has been effectively used to identify and label the electrophilic sites of corrosion inhibitors.[28] While conductive interactions are more likely to occur in the blue (positive) region of the ESP, nucleophilic attacks can occur in the red (negative) region. Fig. 12 shows that the ESP map identifies the anionic group as the primary electrophilic active site. These regions can therefore engage in electron-transferring interactions with the working electrode's surface. Conversely, the areas with the highest positive electrostatic potential are found to be the nitrogen atoms in the [C_nPy]Br molecules.

3.7 Molecular dynamics simulations

In order to better understand the nature and extent of corrosion inhibitor adsorption on metal surfaces, molecular dynamics (MD) simulations offer important insights. The reason this analysis is so popular is that it provides a thorough understanding of the adsorption mechanism and highlights the preferential adsorption sites on the metal surface that result from interatomic interactions between the metal and the inhibitors.[27] As depicted in the equilibrium adsorption model (Fig. 13) for the inhibitor molecule on the Fe(110) crystal surface, no H_2O, H_3O^+, or Cl^- ions are present between the metal surface and the inhibitor. This indicates that the inhibitor displaces the water molecules or other ions previously adsorbed on the surface, forming a strong bond with the metal.

In this study, the Fe(110) surface was chosen for DFT modeling due to its low surface energy and high stability, making it a dominant orientation in bcc Fe. Although real mild steel surfaces are polycrystalline and often partially oxidized, the Fe(110) facet serves as a reasonable approximation to study the intrinsic adsorption and inhibition behavior at the atomic scale.

The MD results for $E_{\text{interaction}}$ and E_{binding} are shown in Table 9, where all three [C_nPy]Br molecules have negative $E_{\text{interaction}}$ values. This suggests that each of these molecules strongly interacts with the Fe(110) surface. The corrosion inhibitor molecule has a greater propensity to contact intimately with the metal surface atoms if its $E_{\text{interaction}}$ value is small.[6,45] The corrosion inhibitor [C_{12}Py]Br shows significant stability on the Fe(110) surface in an acidic media environment with strong contacts, as seen by Table 9, which shows that [C_4Py]Br > [C_8Py]Br > [C_{12}Py]Br, *i.e.*, [C_{12}Py]Br has greater inhibitory properties. One important metric for assessing how strongly corrosion inhibitor molecules connect with metal surfaces is E_{binding}. Table 9 reveals that [C_{12}Py]Br exhibits a high positive value, reflecting its significant adsorption capabilities and high efficacy in corrosion inhibition. The higher E_{binding} of [C_{12}Py]Br (390.473) compared to [C_8Py]Br (343.673) and [C_4Py]Br (315.581)

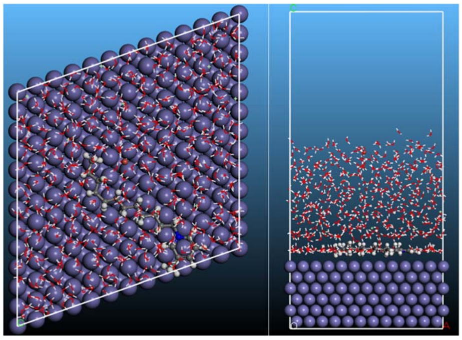

Fig. 13 Side and top views of stabilized adsorption configurations of corrosion inhibitors on the Fe(110) surface.

Table 9 MD simulation results for the adsorption of [C$_n$Py]Br ionic liquids onto the Fe(110) surface in HCl aqueous solutions

Inhibitor	$E_{\text{interaction}}$ (kcal mol^{-1})	E_{binding} (kcal mol^{-1})
[C$_{12}$Py]Br	−390.473	390.473
[C$_8$Py]Br	−343.673	343.673
[C$_4$Py]Br	−315.581	315.581

(Table 9) is attributed to stronger van der Waals interactions between its longer alkyl chain and the Fe(110) surface. This is validated by the RDF (Fig. 15), which shows a peak at 3.0–4.0 Å for C–H⋯Fe interactions—indicating enhanced physical adsorption of longer alkyl chains. Thus, the alkyl chain length directly modulates the hydrophobic barrier effect, a mechanism that cannot be deduced without MD simulations. Fig. 14 illustrates how temperature changes, with smaller E_{binding} values occurring at higher temperatures. This variation can be mainly attributed to the inhibitor compound's decreasing attraction to the metal surface, leading to a repulsive effect as temperature increases.

The radial distribution function (RDF) method is employed to identify chemical bonds, or both bond types, while focusing on the structural analysis of the results obtained from MD simulations.[37] The peaks seen in Fig. 15 can be used to infer the interaction between the Fe(110) surface and the [C$_n$Py]Br ILs. The initial peak, observed within the 1–3.5 Å range, suggests chemical adsorption. This indicates that the N atoms in the [C$_n$Py]Br molecules form strong interactions with the Fe(110) surface through hydrogen bonding or chemical bonding.[59] On the mild steel surface, [C$_n$Py]Br also demonstrates physical adsorption, as evidenced by the peaks observed at a distance of more than 3.5 Å.

3.8 Corrosion inhibition mechanism

The results from both experimental and computational analyses in this study suggest that the adsorption of [C$_n$Py]Br ILs primarily occurs due to the interaction between the inhibitor molecule's active sites and the ionized iron atoms on the metal surface. Fig. 16 shows the possible interactions between the metal surface and the species under investigation in 1 M HCl. Without the presence of inhibitors, chloride ions, owing to their small size and high penetration capacity, are the first to adsorb onto the electrode surface.[51] Subsequently, the adsorbed chloride ions activate the iron atoms, making them more susceptible to oxidation, this process results in the generation of Fe^{2+} ions and speeds up the metal surface's corrosion.

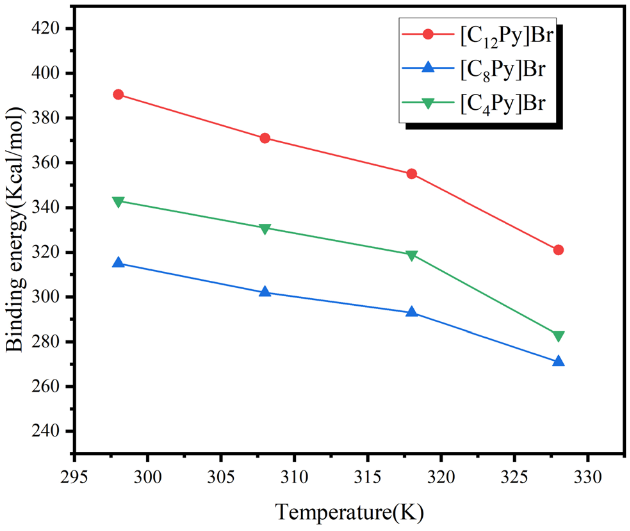

Fig. 14 Calculation of adsorption energy of [C$_{12}$Py]Br ILs on Fe(110) surface in aqueous HCl solution at different temperatures.

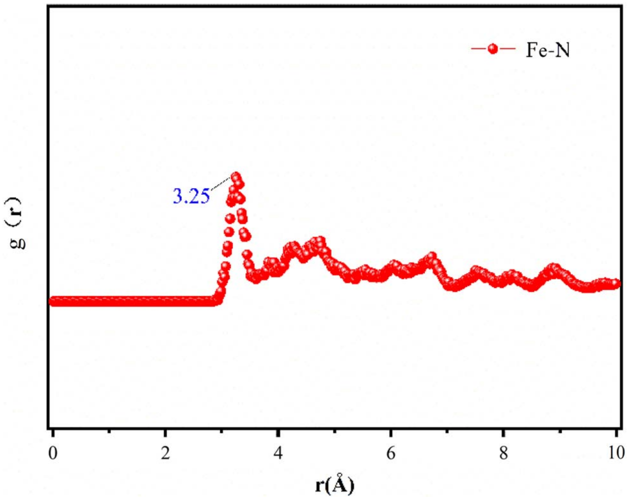

Fig. 15 RDF of [C$_{12}$Py]Br adsorption on Fe(110) surface.

During the corrosion inhibition process, chloride ions (Cl$^-$) initially adsorb onto the metal surface, creating negatively charged regions. These regions attract protonated cations through electrostatic interactions, a mechanism known as physical adsorption. This interaction reduces the active sites available for the cathodic hydrogen evolution reaction, thereby slowing the overall corrosion rate. Inhibitor molecules form coordinate bonds by donating lone pair electrons from their heteroatoms to the vacant d-orbitals of iron. This interaction establishes a protective layer that shields the metal from corrosive environments, with effectiveness influenced by the inhibitor's structure and environmental conditions. In addition, the π-electron clouds on the aromatic ring engage in donor–acceptor interactions (π backbonding) with the ionized Fe atoms on the surface. The combined interaction of donation and π backbonding promotes the creation of protective layers on the metal surface, effectively safeguarding it from corrosion. The large surface area of [C$_{12}$Py]Br promotes the formation of an extensive protective layer, which effectively reduces metal interaction with corrosive environments. The corrosion inhibition mechanism of [C$_n$Py]Br relies on synergism between three functional groups: (1) the pyridinium ring forms coordinate bonds with Fe *via* N → Fe electron donation (chemisorption), confirmed by XPS C–N bonds and DFT HOMO localization. (2) Br$^-$ pre-adsorbs on Fe, creating a negatively charged layer that attracts [C$_n$Py]$^+$ (electrostatic interaction), as supported by EIS Cdl trends and MEP maps. (3) Longer alkyl chains (*e.g.*, C$_{12}$)

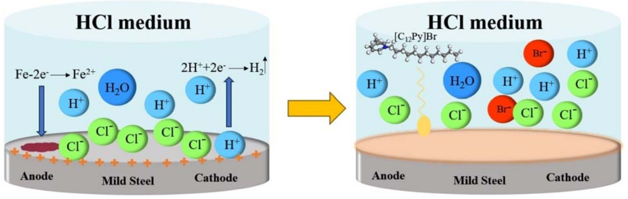

Fig. 16 Mechanism of adsorption of $[C_{12}Py]Br$ molecules on Fe surfaces.

enhance physical adsorption *via* stronger C–H⋯Fe van der Waals interactions (MD RDF data), forming a denser hydrophobic barrier. This multi-functional synergy is novel and cannot be inferred without experimental (weight loss, XPS) and computational (DFT, MD) evidence. Its adsorption properties and molecular structure further enhance its role as a highly efficient corrosion inhibitor.[41,60] When compared with $[C_4Py]Br$ and $[C_8Py]Br$, this is probably the main reason why this molecule exhibits better inhibitory activity.

4 Conclusion

(1) Weight-loss test shows that within a certain concentration range, the corrosion inhibition efficiency increases with the increase of corrosion inhibitor concentration and reaches a steady state at the optimal concentration point. The study also found that an increase in temperature can have a negative impact on corrosion inhibition efficiency, leading to a decrease in it. Under the same concentration conditions, comparative tests of different types of corrosion inhibitors show that the performance of $[C_{12}Py]$ Br is superior to that of $[C_8Py]$ Br and $[C_4Py]$ Br.

(2) Electrochemical testing revealed that the three added ILs corrosion inhibitors can effectively reduce the corrosion current density in acidic corrosive media, indicating their significant corrosion inhibition performance. In acidic environments, these ILs corrosion inhibitors act as mixed corrosion inhibitors; in acidic media, the corrosion inhibitor achieved a maximum inhibition efficiency of 94.1%. The adsorption behavior of all ILs corrosion inhibitors follows the Langmuir isotherm adsorption model. The Gibbs free energy analysis of corrosion inhibitor adsorption reveals that its adsorption mechanism is a combination of physical and chemical adsorption.

(3) The results of surface analysis technology show that the samples with added corrosion inhibitors exhibit significant corrosion inhibition effects, and trace element analysis confirms the formation of a protective corrosion inhibitor film on the surface of low carbon steel. XPS further confirmed the binding effect of physical adsorption and chemical adsorption by detecting the composition of the sample surface.

(4) The quantum chemistry calculation results indicate that the electrons of the three ILs corrosion inhibitors are mainly concentrated on nitrogen atoms, which helps to determine the adsorption sites on the surface of low carbon steel, and further supports the experimental results through the analysis of frontier orbital distribution and reaction activity. The molecular dynamics simulation results indicate that ILs can form stable adsorption on the surface of low carbon steel through interfacial donor acceptor interactions, and the inhibition sequence obtained from the binding energy results is consistent with the experimental results. Notably, our work clarifies the distinct roles of the pyridinium ring (chemical adsorption), Br^- (electrostatic pre-adsorption), and alkyl chain (physical barrier) in $[C_nPy]Br$—revealing a synergistic mechanism unreported in prior studies. Key findings (*e.g.*, the critical role of C_{12} alkyl chain and C–N bond formation) depend on experimental data and calculations, as they cannot be intuitively deduced. The radial distribution function (RDF) calculation confirmed that the adsorption type is a mixed adsorption mainly composed of chemical adsorption and supplemented by physical adsorption.

Data availability

The data that support the findings of this study are available upon reasonable request. Requests for access to the data should be directed to the corresponding author. The authors are committed to transparency and open science practices and will make every effort to provide the necessary data for validation and replication of the results presented in this paper.

Author contributions

Data curation, Jiale Zhang; project administration, Pei Yao; supervision, Entian Li; writing – original draft, Fang Luo; writing – review & editing, Fang Luo.

Conflicts of interest

The authors declare that they have no known competing financial interests or personal relationships that could have appeared to influence the work reported in this paper.

References

1 A. Nahlé, R. Salim, F. E. Hajjaji, E. Ech-Chihbi, A. Titi, M. Messali, S. Kaya, B. El Ibrahimi and M. Taleb, Experimental and theoretical approach for novel imidazolium ionic liquids as Smart Corrosion inhibitors for mild steel in 1.0 M hydrochloric acid, *Arabian J. Chem.*, 2022, **15**, 103967, DOI: **10.1016/j.arabjc.2022.103967**.

2 S. H. M. Jessima, S. Subhashini, A. Berisha, V. Mehmeti and S. S. Srikandan, Experimental and Theoretical Approach of Evaluating Chitosan Ferulic Acid Amide As An Effective Corrosion Inhibitor, *J. Bio Tribo Corros.*, 2021, **9**, 80, DOI: **10.21203/rs.3.rs-161633/v1**.

3 E. Li, J. Zhang, B. Wang and P. Yao, Combined electrochemical, surface analysis and DFT/MD-simulations to evaluate choline histidine ionic liquid as a green corrosion inhibitor for mild steel in neutral medium, *Mater. Today Commun.*, 2024, 109871, DOI: **10.1016/j.mtcomm.2024.109871**.

4 C. Wang, J. Chen, B. Hu, Z. Liu, C. Wang, J. Han, M. Su, Y. Li and C. Li, Modified chitosan-oligosaccharide and sodium

silicate as efficient sustainable inhibitor for carbon steel against chloride-induced corrosion, *J. Clean. Prod.*, 2019, **238**, 117823, DOI: **10.1016/j.jclepro.2019.117823**.

5 E. Berdimurodov, A. Kholikov, K. Akbarov, L. Guo, S. Kaya, K. P. Katin, D. Kumar Verma, M. Rbaa, O. Dagdag and R. Haldhar, Novel bromide–cucurbit[7]uril supramolecular ionic liquid as a green corrosion inhibitor for the oil and gas industry, *J. Electroanal. Chem.*, 2021, **901**, 115794, DOI: **10.1016/j.jelechem.2021.115794**.

6 M.-F. Chen, Y. Chen, Z. Jia Lim and M. Wah Wong, Adsorption of imidazolium-based ionic liquids on the Fe(100) surface for corrosion inhibition: Physisorption or chemisorption?, *J. Mol. Liq.*, 2022, **367**, 120489, DOI: **10.1016/j.molliq.2022.120489**.

7 B. El Ibrahimi, A. Jmiai, L. Bazzi and S. El Issami, Amino acids and their derivatives as corrosion inhibitors for metals and alloys, *Arabian J. Chem.*, 2020, **13**, 740–771, DOI: **10.1016/j.arabjc.2017.07.013**.

8 Y. L. Kobzar and K. Fatyeyeva, Ionic liquids as green and sustainable steel corrosion inhibitors: Recent developments, *Chem. Eng. J.*, 2021, **425**, 131480, DOI: **10.1016/j.cej.2021.131480**.

9 M. Cui, Z. Wang and B. Wang, Survival strategies of mangrove (Ceriops tagal (Perr.) CB Rob) and the inspired corrosion inhibitor, *Front. Mater.*, 2022, **9**, 879525, DOI: **10.3389/fmats.2022.879525**.

10 M. T. Zaky, M. I. Nessim and M. A. Deyab, Synthesis of new ionic liquids based on dicationic imidazolium and their anti-corrosion performances, *J. Mol. Liq.*, 2019, **290**, 111230, DOI: **10.1016/j.molliq.2019.111230**.

11 S. Shuncun, Y. Pinggui, C. Chenzhong, W. Xueye, S. Jieshu and L. Junxi, Synthesis of new ionic liquids and corrosion inhibition performance of its cationic imidazoline group, *J. Chem. Ind. Eng.*, 2005, **56**, 1112.

12 F. A. Azeez, O. A. Al-Rashed and A. A. Nazeer, Controlling of mild-steel corrosion in acidic solution using environmentally friendly ionic liquid inhibitors: Effect of alkyl chain, *J. Mol. Liq.*, 2018, **265**, 654–663, DOI: **10.1016/j.molliq.2018.05.093**.

13 A. Bousskri, A. Anejjar, M. Messali, R. Salghi, O. Benali, Y. Karzazi, S. Jodeh, M. Zougagh, E. E. Ebenso and B. Hammouti, Corrosion inhibition of carbon steel in aggressive acidic media with 1-(2-(4-chlorophenyl)-2-oxoethyl) pyridazinium bromide, *J. Mol. Liq.*, 2015, **211**, 1000–1008.

14 A. A. Moustafa, S. M. Abdelbasir, A. M. Ashmawy, I. M. Ghayad and A. A. El-Zomrawy, A novel ionic liquid for improvement of lead-acid battery performance and protection of its electrodes against corrosion, *Mater. Chem. Phys.*, 2022, **292**, 126764, DOI: **10.1016/j.matchemphys.2022.126764**.

15 M. Brunner, H. Li, Z. Zhang, D. Zhang and R. Atkin, Pinewood pyrolysis occurs at lower temperatures following treatment with choline-amino acid ionic liquids, *Fuel*, 2019, **236**, 306–312, DOI: **10.1016/j.fuel.2018.09.004**.

16 S. H. Alrefaee, Effect of alkyl chain length and halide ions on the corrosion inhibition potential of imidazolium and pyridinium based ionic liquids: Computational studies, *J. Mol. Liq.*, 2021, **344**, 117848.

17 D. Pharma, A. Bousskri, R. Salghi, A. Anejjar and M. Zougagh, Pyridazinium-based ionic liquids as corrosion inhibitors for copper inphosphoric acid containing chloride: electrochemical, surface and quantumchemical comparatives studies, *Pharma Chem.*, 2016, **8**, 67–83.

18 A. Husain, A. A. Adewunmi, M. S. Kamal, M. Mahmoud and M. A. J. E. Al-Harthi, Demulsification of Heavy Petroleum Emulsion Using Pyridinium Ionic Liquids with Distinct Anion Branching, *Energy Fuels*, 2021, **35**, 16527–16533.

19 Q. Liu, Y. Cao, M. Zhou, Z. Miao, J. Yang, Z. Du, B. Lu, G. Liu, J. Li and S. J. C. Chen, Efficient Recycling and Utilization Strategy for Steel Spent Pickling Solution, *Coatings*, 2024, **14**, 784.

20 E. Kamali Ardakani, E. Kowsari and A. Ehsani, Imidazolium-derived polymeric ionic liquid as a green inhibitor for corrosion inhibition of mild steel in 1.0 M HCl: Experimental and computational study, *Colloids Surf., A*, 2020, **586**, 124195, DOI: **10.1016/j.colsurfa.2019.124195**.

21 C. Verma, I. B. Obot, I. Bahadur, E.-S. M. Sherif and E. E. Ebenso, Choline based ionic liquids as sustainable corrosion inhibitors on mild steel surface in acidic medium: Gravimetric, electrochemical, surface morphology, DFT and Monte Carlo simulation studies, *Appl. Surf. Sci.*, 2018, **457**, 134–149, DOI: **10.1016/j.apsusc.2018.06.035**.

22 P. Wang, Q. Lv, Y. Tao, L. Cheng, R. Li, Y. Jiao, C. Fang, H. Li, C. Geng, C. Sun, J. Ding, H. Wan and G. Guan, One-pot efficient fixation of low-concentration CO2 into cyclic carbonate by mesoporous pyridine-functionalized binuclear poly(ionic liquid)s, *Mol. Catal.*, 2023, **544**, 113157, DOI: **10.1016/j.mcat.2023.113157**.

23 J. Wu, S. Wan, O. Xu, H. Song, J. Yang and X. Zhu, Pyridine ionic liquid functionalized bimetallic MOF solid-phase extraction coupled with high performance liquid chromatography for separation/analysis sunset yellow, *RSC Adv.*, 2022, **12**, 30928–30935, DOI: **10.1039/d2ra05980k**.

24 L. Peng, S. Wang, X. Wang, J. Gao, D. Xu, L. Zhang and Y. Wang, Liquid-liquid extraction and mechanism exploration for separation of mixture 2,2,3,3-Tetrafluoro-1-propanol and water using pyridine-based ionic liquids, *J. Mol. Liq.*, 2022, **360**, 119468, DOI: **10.1016/j.molliq.2022.119468**.

25 K. Cao, W. Huang, X. Huang and J. Pan, Imidazo [1, 2-a] pyrimidine derivatives as effective inhibitor of mild steel corrosion in HCl solution: Experimental and theoretical studies, *Front. Mater.*, 2022, **9**, 843522, DOI: **10.3389/fmats.2022.843522**.

26 A. Yazdani, M. Sivapragasam, J. M. Leveque and M. Moniruzzaman, Microbial biocompatibility and biodegradability of choline-amino acid based ionic liquids, *J. Microb. Biochem. Technol.*, 2016, **8**, 415–421, DOI: **10.4172/1948-5948.1000318**.

27 G. Parveen, S. Bashir, A. Thakur, S. K. Saha, P. Banerjee and A. Kumar, Experimental and computational studies of imidazolium based ionic liquid 1-methyl- 3-

propylimidazolium iodide on mild steel corrosion in acidic solution, *Mater. Res. Express*, 2019, **7**, 016510, DOI: 10.1088/2053-1591/ab5c6a.

28 E. Li, S. Liu, F. Luo and P. Yao, Amino acid imidazole ionic liquids as green corrosion inhibitors for mild steel in neutral media: Synthesis, electrochemistry, surface analysis and theoretical calculations, *J. Electroanal. Chem.*, 2023, **944**, 117650, DOI: 10.1016/j.jelechem.2023.117650.

29 R. Aslam, M. Mobin, Huda, I. B. Obot and A. H. Alamri, Ionic liquids derived from α-amino acid ester salts as potent green corrosion inhibitors for mild steel in 1M HCl, *J. Mol. Liq.*, 2020, **318**, 113982, DOI: 10.1016/j.molliq.2020.113982.

30 M. Mobin, Huda, S. Zamindar and P. Banerjee, Mechanistic insight into adsorption and anti-corrosion capability of a novel surfactant-derived ionic liquid for mild steel in HCl medium, *J. Mol. Liq.*, 2023, **385**, 122403, DOI: 10.1016/j.molliq.2023.122403.

31 X. Zhang, Y. Zhang, Y. Su and S. Guan, Enhancing the corrosion inhibition performance of Mannich base on mild steel in lactic acid solution through synergistic effect of allicin: Experimental and theoretical study, *J. Mol. Struct.*, 2024, **1304**, 137658, DOI: 10.1016/j.molstruc.2024.137658.

32 R. Solmaz, A. Salcı, Y. A. Dursun and G. Kardaş, A comprehensive study on the adsorption, corrosion inhibition efficiency and stability of acriflavine on mild steel in 1 M HCl solution, *Colloids Surf., A*, 2023, **674**, 131908, DOI: 10.1016/j.colsurfa.2023.131908.

33 D. I. Udunwa, O. D. Onukwuli, M. C. Menkiti, V. C. Anadebe and M. A. Chidiebere, 1-Butyl-3-methylimidazolium methane sulfonate ionic liquid corrosion inhibitor for mild steel alloy: Experimental, optimization and theoretical studies, *Heliyon*, 2023, **9**, e18353, DOI: 10.1016/j.heliyon.2023.e18353.

34 F. E. Abeng and V. C. Anadebe, Combined electrochemical, DFT/MD-simulation and hybrid machine learning based on ANN-ANFIS models for prediction of doxorubicin drug as corrosion inhibitor for mild steel in 0.5 M H2SO4 solution, *Comput. Theor. Chem.*, 2023, **1229**, 114334, DOI: 10.1016/j.comptc.2023.114334.

35 H. Jia, Q. Wang, H. Yan, G. Wu, J. Li, Z. Shen, H. Sun, P. Pei, H. Jia and D. Liu, Investigation of phosphorus-based ionic liquid with long alkyl chain as high-performance corrosion inhibitor with ultralow concentration for mild steel in 1 M HCl solution, *J. Mol. Liq.*, 2024, **396**, 123946, DOI: 10.1016/j.molliq.2023.123946.

36 J. Wen, X. Zhang, Y. Liu, B. Shang, J. He and L. Li, Exploration of imidazol-4-methylimine thiourea as effective corrosion inhibitor for mild steel in hydrochloric medium: Experimental and theoretical studies, *Colloids Surf., A*, 2023, **674**, 131895, DOI: 10.1016/j.colsurfa.2023.131895.

37 F. E. L. Hajjaji, R. Salim, E. Ech-chihbi, A. Titi, M. Messali, S. Kaya, B. E. Ibrahimi and M. Taleb, New imidazolium ionic liquids as ecofriendly corrosion inhibitors for mild steel in hydrochloric acid (1 M): Experimental and theoretical approach, *J. Taiwan Inst. Chem. Eng.*, 2021, **123**, 346–362, DOI: 10.1016/j.jtice.2021.05.005.

38 L. N. Emembolu, P. E. Ohale, C. E. Onu and N. J. Ohale, Comparison of RSM and ANFIS modeling techniques in corrosion inhibition studies of Aspilia Africana leaf extract on mild steel and aluminium metal in acidic medium, *Appl. Surf. Sci. Adv.*, 2022, **11**, 100316, DOI: 10.1016/j.apsadv.2022.100316.

39 R. Salim, E. Ech-chihbi, Y. Fernine, M. Koudad, L. Guo, E. Berdimurodov, M. Azam, Z. Rais and M. Taleb, Inhibition behavior of new ecological corrosion inhibitors for mild steel, copper and aluminum in acidic environment: Theoretical and experimental investigation, *J. Mol. Liq.*, 2024, **393**, 123579, DOI: 10.1016/j.molliq.2023.123579.

40 E. Li, Y. Li, S. Liu and P. Yao, Choline amino acid ionic liquids as green corrosion inhibitors of mild steel in acidic medium, *Colloids Surf., A*, 2023, **657**, 130541, DOI: 10.1016/j.colsurfa.2022.130541.

41 S. Ullah, M. A. Bustam, A. M. Shariff, G. Gonfa and K. Izzat, Experimental and quantum study of corrosion of A36 mild steel towards 1-butyl-3-methylimidazolium tetrachloroferrate ionic liquid, *Appl. Surf. Sci.*, 2016, **365**, 76–83, DOI: 10.1016/j.apsusc.2015.12.232.

42 L. Feng, S. Zhang, Y. Lu, B. Tan, S. Chen and L. Guo, Synergistic corrosion inhibition effect of thiazolyl-based ionic liquids between anions and cations for copper in HCl solution, *Appl. Surf. Sci.*, 2019, **483**, 901–911, DOI: 10.1016/j.apsusc.2019.03.299.

43 A. Toghan, O. K. Alduaij, A. Fawzy, A. M. Mostafa, A. M. Eldesoky and A. A. Farag, Effect of Adsorption and Interactions of New Triazole-Thione-Schiff Bases on the Corrosion Rate of Carbon Steel in 1 M HCl Solution: Theoretical and Experimental Evaluation, *ACS Omega*, 2024, **9**, 6761–6772, DOI: 10.1021/acsomega.3c08127.

44 J. Aslam, C. Verma and R. Aslam, *Grafted Biopolymers as Corrosion Inhibitors: Safety, Sustainability, and Efficiency*, John Wiley & Sons, 2023.

45 S. K. Saha and P. Banerjee, Introduction of newly synthesized Schiff base molecules as efficient corrosion inhibitors for mild steel in 1 M HCl medium: an experimental, density functional theory and molecular dynamics simulation study, *Mater. Chem. Front.*, 2018, **2**, 1674–1691, DOI: 10.1039/C8QM00162F.

46 T. S. Hamidon and M. H. Hussin, Susceptibility of hybrid sol-gel (TEOS-APTES) doped with caffeine as potent corrosion protective coatings for mild steel in 3.5 wt.% NaCl, *Prog. Org. Coat.*, 2020, **140**, 105478, DOI: 10.1016/j.porgcoat.2019.105478.

47 F. El Hajjaji, E. Ech-chihbi, R. Salim, A. Titi, M. Messali, B. El Ibrahimi, S. Kaya and M. Taleb, A detailed electronic-scale DFT modeling/MD simulation, electrochemical and surface morphological explorations of imidazolium-based ionic liquids as sustainable and non-toxic corrosion inhibitors for mild steel in 1 M HCl, *Mater. Sci. Eng., B*, 2023, **289**, 116232, DOI: 10.1016/j.mseb.2022.116232.

48 L. Zhang, L. Li, D. Shi, X. Peng, F. Song, F. Nie and W. Han, Recovery of lithium from alkaline brine by solvent extraction

with β-diketone, *Hydrometallurgy*, 2018, **175**, 35–42, DOI: 10.1016/j.hydromet.2017.10.029.

49 P. Kannan, A. Varghese, K. Palanisamy and A. S. Abousalem, Probing the effect of newly synthesized phenyltrimethylammonium tetrachloroaluminate ionic liquid as an inhibitor for carbon steel corrosion, *Appl. Surf. Sci. Adv.*, 2021, **6**, 100150, DOI: 10.1016/j.apsadv.2021.100150.

50 R. K. Mehta and M. Yadav, Corrosion inhibition properties of expired Broclear medicine and its carbon dot as eco-friendly inhibitors for mild steel in 15% HCl, *Mater. Sci. Eng., B*, 2023, **295**, 116566, DOI: 10.1016/j.mseb.2023.116566.

51 R. Aslam, J. Zhao, X. Sun, X. Zhou, Q. Wang, J. Aslam and Z. Yan, Bio-based ionic liquid as a corrosion inhibitor for mild steel in 5% HCl solution: Experimental and theoretical investigation, *Sustainable Chem. Pharm.*, 2024, **39**, 101614, DOI: 10.1016/j.scp.2024.101614.

52 Z. Zhang, X. Huang, N. Tian, F. Ni, L. Ruan, Y. Lv and L. Wu, Corrosion Inhibition Effect of Histidine and Its Derivatives Self-Assembled Films Formed of 304 Stainless Steel, *Int. J. Electrochem. Sci.*, 2016, **11**, 9175–9191, DOI: 10.20964/2016.11.73.

53 H. Yan, S. Dai, P. Liu and Y. Zhu, Synergistic mechanism of ternary green corrosion inhibitors for N80 steel in 20 wt% HCl solution: Encapsulation and transportation of vanillin through micelles formed by ionic liquids, *Corros. Sci.*, 2024, **227**, 111750, DOI: 10.1016/j.corsci.2023.111750.

54 Z. Huang, Y. ChenYang, X. Wang, R. Cai and B. Han, Biodiesel synthesis through soybean oil transesterification using choline-based amino acid ionic liquids as catalysts, *Ind. Crops Prod.*, 2024, **208**, 117869, DOI: 10.1016/j.indcrop.2023.117869.

55 J. Zhang, M. Kong, J. Feng, C. Yin, D. Li, L. Fan, Q. Chen and H. Liu, Dimeric imidazolium ionic liquids connected by bipyridiyl as a corrosion inhibitor for N80 carbon steel in HCl, *J. Mol. Liq.*, 2021, **344**, 117962, DOI: 10.1016/j.molliq.2021.117962.

56 P. Wang, J. Qiu, P. Gao, R. Dong, Y. Han and M. Fan, The tribological behaviors and anti-corrosion performances of 5-phenyltetrazole ionic liquid additives for water lubricants, *Wear*, 2023, **516–517**, 204621, DOI: 10.1016/j.wear.2023.204621.

57 Z. Zhang, K. Fukami, W. Liu, W. Liu and K. Murase, Simultaneously enhancing mechanical and anti-corrosion properties of aluminum through electrodeposition of supersaturated Al(Fe) solid solutions, *Appl. Surf. Sci.*, 2024, **671**, 160748, DOI: 10.1016/j.apsusc.2024.160748.

58 Y. Wu, X. Zhong, D. Hong, R. Liang, D. Fan, Y. Niu and X. Zheng, Corrosion behaviors of Lu4Hf3O12 thermal/environmental barrier coatings to molten CMAS attack at 1300–1500 °C, *Appl. Surf. Sci.*, 2024, **676**, 161020, DOI: 10.1016/j.apsusc.2024.161020.

59 M. Marczewski, W. Tylus and J. Winiarski, The effect of anodic polarization parameters of 316L steel in a propylene glycol: Choline chloride eutectic solvent on surface finishing, chemistry and corrosion resistance, *Appl. Surf. Sci.*, 2024, **652**, 159335, DOI: 10.1016/j.apsusc.2024.159335.

60 P. Li, Z. Li, S. Liu, C. Li, L. Ma, C. Yang, D. Han, C. Niu, X. Xin and F. Li, Imidazole/pyridine-based ionic liquids modified metal-organic frameworks for efficient adsorption of Congo red in water, *J. Mol. Struct.*, 2024, **1303**, 137599, DOI: 10.1016/j.molstruc.2024.137599.